

A: Kinetics, Dynamics, Photochemistry, and Excited States

Acetonyl Peroxy and Hydro Peroxy Self- and Cross-Reactions: Kinetics, Mechanism, and Chaperone Enhancement from the Perspective of the Hydroxyl Radical Product

Kristen Zuraski, Aileen O. Hui, Fred J. Grieman, Emily Darby, Kristian H. Møller, Frank A. F. Winiberg, Carl J. Percival, Matthew D. Smarte, Mitchio Okumura, Henrik Grum Kjaergaard, and Stanley P Sander

J. Phys. Chem. A, **Just Accepted Manuscript** • DOI: 10.1021/acs.jpca.0c06220 • Publication Date (Web): 27 Aug 2020

Downloaded from pubs.acs.org on August 27, 2020

Just Accepted

“Just Accepted” manuscripts have been peer-reviewed and accepted for publication. They are posted online prior to technical editing, formatting for publication and author proofing. The American Chemical Society provides “Just Accepted” as a service to the research community to expedite the dissemination of scientific material as soon as possible after acceptance. “Just Accepted” manuscripts appear in full in PDF format accompanied by an HTML abstract. “Just Accepted” manuscripts have been fully peer reviewed, but should not be considered the official version of record. They are citable by the Digital Object Identifier (DOI®). “Just Accepted” is an optional service offered to authors. Therefore, the “Just Accepted” Web site may not include all articles that will be published in the journal. After a manuscript is technically edited and formatted, it will be removed from the “Just Accepted” Web site and published as an ASAP article. Note that technical editing may introduce minor changes to the manuscript text and/or graphics which could affect content, and all legal disclaimers and ethical guidelines that apply to the journal pertain. ACS cannot be held responsible for errors or consequences arising from the use of information contained in these “Just Accepted” manuscripts.

Acetonyl Peroxy and Hydro Peroxy Self- and Cross- Reactions: Kinetics, Mechanism, and Chaperone Enhancement from the Perspective of the Hydroxyl Radical Product

Kristen Zuraski,^a Aileen O. Hui,^{b,c} Fred J. Grieman,^{*,a,d} Emily Darby,^{a,d,e} Kristian H. Møller,^f Frank A. F. Winiberg,^a Carl J. Percival,^a Matthew D. Smarte,^b Mitchio Okumura,^b Henrik G. Kjaergaard,^{*,f} and Stanley P. Sander^{*,a}

^aNASA Jet Propulsion Laboratory, California Institute of Technology, 4800 Oak Grove Drive, Pasadena, California 91109, United States

^bArthur Amos Noyes Laboratory of Chemical Physics, California Institute of Technology, Pasadena, California 91125, United States

^cnow at: The Aerospace Corporation, El Segundo, California 90245, United States

^dSeaver Chemistry Laboratory, Pomona College, Claremont, California 91711, United States

^enow at: Trussell Technologies, Oakland, California 94612, United States

^fDepartment of Chemistry, University of Copenhagen, Universitetsparken 5, DK-2100 Copenhagen Ø, Denmark

Corresponding Authors

*fjg04747@pomona.edu (F.J.G); hgk@chem.ku.dk (H.G.K); stanley.p.sander@jpl.nasa.gov (S.P.S.).

© 2020. All rights reserved.

ABSTRACT

Pulsed laser photolysis coupled with infrared (IR) wavelength modulation spectroscopy and ultraviolet (UV) absorption spectroscopy was used to study the kinetics and branching fractions for the acetyl peroxy ($\text{CH}_3\text{C}(\text{O})\text{CH}_2\text{O}_2$) self-reaction and its reaction with hydro peroxy (HO_2) at a temperature of 298 K and pressure of 100 Torr. Near-IR and mid-IR lasers simultaneously monitored HO_2 and hydroxyl, OH, respectively, while UV absorption measurements monitored the $\text{CH}_3\text{C}(\text{O})\text{CH}_2\text{O}_2$ concentrations. The overall rate constant for the reaction between $\text{CH}_3\text{C}(\text{O})\text{CH}_2\text{O}_2$ and HO_2 was found to be $(5.5 \pm 0.5) \times 10^{-12} \text{ cm}^3 \text{ molecule}^{-1} \text{ s}^{-1}$ and the branching fraction for OH yield from this reaction was directly measured as 0.30 ± 0.04 . The $\text{CH}_3\text{C}(\text{O})\text{CH}_2\text{O}_2$ self-reaction rate constant was measured to be $(4.8 \pm 0.8) \times 10^{-12} \text{ cm}^3 \text{ molecule}^{-1} \text{ s}^{-1}$ and the branching fraction for alkoxy formation was inferred from secondary chemistry as 0.33 ± 0.13 . An increase in the rate of the HO_2 self-reaction was also observed as a function of acetone ($\text{CH}_3\text{C}(\text{O})\text{CH}_3$) concentration which is interpreted as a chaperone effect resulting from hydrogen-bond complexation between HO_2 and $\text{CH}_3\text{C}(\text{O})\text{CH}_3$. The chaperone enhancement coefficient for $\text{CH}_3\text{C}(\text{O})\text{CH}_3$ was determined to be $k''_{\text{A}} = (4.0 \pm 0.2) \times 10^{-29} \text{ cm}^6 \text{ molecule}^{-2} \text{ s}^{-1}$ and the equilibrium constant for $\text{HO}_2 \bullet \text{CH}_3\text{C}(\text{O})\text{CH}_3$ complex formation was found to be $K_{\text{c}}(\text{R15}) = (2.0 \pm 0.89) \times 10^{-18} \text{ cm}^3 \text{ molecule}^{-1}$; from these values the rate constant for the $\text{HO}_2 + \text{HO}_2 \bullet \text{CH}_3\text{C}(\text{O})\text{CH}_3$ reaction was estimated to be $(2 \pm 1) \times 10^{-11} \text{ cm}^3 \text{ molecule}^{-1} \text{ s}^{-1}$. Results from UV absorption cross-section measurements of $\text{CH}_3\text{C}(\text{O})\text{CH}_2\text{O}_2$ and prompt OH radical yields arising from possible oxidation of the $\text{CH}_3\text{C}(\text{O})\text{CH}_3$ -derived alkyl radical are also discussed. Using theoretical methods, no likely pathways for the observed prompt OH radical formation have been found and thus remains unexplained.

I. INTRODUCTION

Atmospheric oxidation of volatile organic compounds (VOCs, RH) leads to the formation of organic peroxy radicals, RO_2 . These species play a vital role in the budgets of O_3 , NO_x ($NO + NO_2$), NO_y ($NO_x + NO_z$; $NO_z = HNO_3, HONO, PAN + \text{other nitrogen oxides}$), and HO_x ($OH + HO_2$) throughout the troposphere and, consequently, are important in determining atmospheric composition, the Earth's radiative balance and future changes in climate. Once formed, RO_2 can react with NO_x , HO_2 (R1), OH , other $R'O_2$ species/itself (R2), or undergo H-shift reactions to form autoxidation products (R3) as shown in Figure 1.¹⁻¹⁰

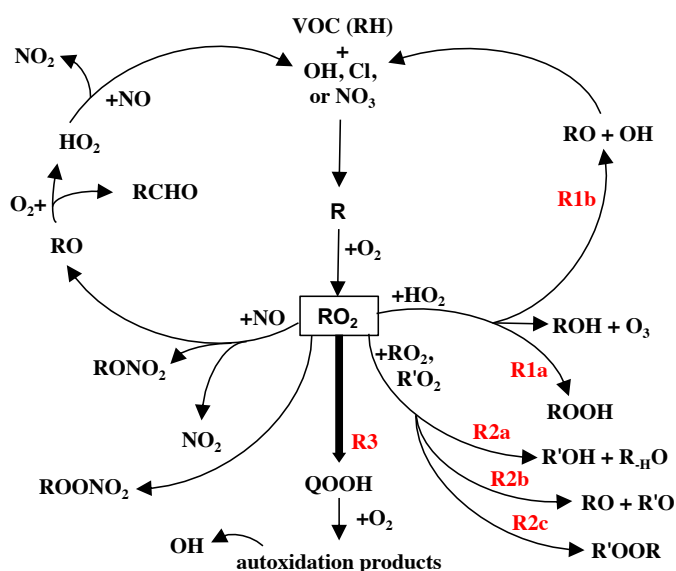
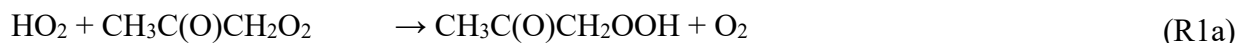


Figure 1. General scheme for RO_2 chemistry in the atmosphere.^{1,2} The right and left side represent low and high NO_x environments, respectively. The bold arrow indicates unimolecular rearrangement by H-shift reactions.

In pristine environments, direct emissions from vegetation, oxidation of anthropogenic and biogenic hydrocarbons, oceans, and biomass burning make acetone, $CH_3C(O)CH_3$, one of the most abundant oxygenated VOCs in the atmosphere.¹¹⁻¹⁴ Following oxidation of $CH_3C(O)CH_3$ to form acetyl peroxy, $CH_3C(O)CH_2O_2$, reactions with hydro peroxy, HO_2 , dominate in low NO_x environments and impact the HO_x balance by removing HO_2 and working as either a HO_x radical sink through the formation of hydroperoxides ($ROOH$, R1a) or as radical

propagation by generating hydroxyl radicals (OH, R1b).¹⁵⁻²¹ The ozone generating pathway shown in Figure 1 is not available for CH₃C(O)CH₂O₂ due to the position of the carbonyl group.¹⁶



The importance of accurately accounting for the OH production from peroxy radical reactions (R1b, in Fig. 1) is driven in part by OH field measurements in pristine environments which report elevated mixing ratios compared with atmospheric models.²²⁻²⁵ OH-recycling from peroxy radical reactions as well as autoxidation reactions may explain, in part, the discrepancy between measurements and models.

Additional fates of the CH₃C(O)CH₂O₂ radical in pristine environments include reactions with other peroxy radicals and with itself. These reactions are less dominating in the atmosphere compared to reactions with NO_x and HO₂, but are important for laboratory studies. Similar to other peroxy radicals, there are two established self-reaction pathways for CH₃C(O)CH₂O₂: one which leads to hydroxyacetone (CH₃C(O)CH₂OH) and methylglyoxal (CH₃C(O)CHO) as stable products (R2a) and the other that generates acetonoxyl radical (CH₃C(O)CH₂O, R2b).^{21, 26, 27} In addition, a third pathway, R2c, was recently proposed and observed by Berndt et al., which leads to higher functionalized accretion products, ROOR.²⁸



Previously, the cross-reaction rate constant for CH₃C(O)CH₂O₂ + HO₂ (*k*₁) has only been measured once by Bridier et al.²¹ using flash photolysis and ultraviolet (UV) absorption of

1
2
3 CH₃C(O)CH₂O₂ and other radicals. As with all spectroscopic studies, the experimentally
4
5 determined rate constant is highly sensitive to the values of the UV absorption cross-sections
6
7 employed. However, the reported literature values of UV absorption cross-section for
8
9 CH₃C(O)CH₂O₂ radical, $\sigma_{\text{CH}_3\text{C}(\text{O})\text{CH}_2\text{O}_2}$, are not in good agreement and vary by up to a factor of
10
11 2.5.^{21, 26, 29} The k_1 rate constant from the Bridier et al.²¹ study was determined using much larger
12
13 $\sigma_{\text{CH}_3\text{C}(\text{O})\text{CH}_2\text{O}_2}$ values compared to other literature works. In subsequent studies, their value for k_1
14
15 was used to determine the branching fraction for OH formation,^{15, 18-20} which propagated any
16
17 error in their reported k_1 to the reported branching fraction values. The literature values for the
18
19 branching fraction of the OH generating channel, k_{1b}/k_1 , are not in agreement, ranging from 0.15
20
21 – 0.67. A single theoretical study by Hasson et al.¹⁶ of the branching between R1a and R1b finds
22
23 that R1a is favored, but lowering the energy of the CH₃C(O)CH₂O₂•HO₂ intermediate complex
24
25 by just 2 kcal mol⁻¹ inverts the branching to favor R1b demonstrating the sensitivity of the
26
27 branching fraction to the energies determined in the structure calculations. None of these
28
29 experimental or theoretical studies have considered H-shift isomerization reactions.
30
31
32
33
34
35

36 The rate constant for the CH₃C(O)CH₂O₂ self-reaction (k_2) has been measured by two
37
38 studies^{21, 26} that are in agreement but with one only reporting an upper limit²⁶. This agreement
39
40 may be fortuitous, however, because significantly different $\sigma_{\text{CH}_3\text{C}(\text{O})\text{CH}_2\text{O}_2}$ were used between
41
42 these two studies. Subsequent indirect observation of the branching fraction of k_{2b}/k_2 by Emricha
43
44 and Warneck³⁰ did not agree with the results by Bridier et al.²¹ showing a difference of 0.25. The
45
46 most recent results by Berndt et al.²⁸ measured k_{2c} only and based the branching fraction for this
47
48 channel on the results of the previous studies.
49
50
51

52 Our work is the first study to monitor simultaneously the time-dependent concentration
53
54 profiles for CH₃C(O)CH₂O₂, HO₂, and OH independently. The goal of this work is to reassess
55
56
57
58
59
60

1
2
3 and resolve the discrepancies in the overall kinetic rate constants, k_1 and k_2 , and the associated
4
5 branching fractions. We have re-measured $\sigma_{\text{CH}_3\text{C}(\text{O})\text{CH}_2\text{O}_2}$ at selected wavelengths in the region
6
7 between 290 – 320 nm and constrained the results of our kinetic model fits by coupling the
8
9 kinetic data of $\text{CH}_3\text{C}(\text{O})\text{CH}_2\text{O}_2$ with HO_2 and OH , both obtained through infrared wavelength
10
11 modulated spectroscopy (IR-WMS). In addition, a significant chaperone effect caused by
12
13 $\text{CH}_3\text{C}(\text{O})\text{CH}_3$ forming a hydrogen-bonded (H-bonded) complex with HO_2 that, in turn, increases
14
15 the HO_2 self-reaction rate was also observed at room temperature and is reported here for the
16
17 first time. This HO_2 self-reaction rate enhancement must be included in the analysis to obtain
18
19 accurate kinetic parameters for the $\text{CH}_3\text{C}(\text{O})\text{CH}_2\text{O}_2$ chemistry.
20
21
22
23

24 **II. METHODS**

25 **IIa. Experimental**

26 **Infrared Kinetic Spectroscopy (IRKS)**

27
28 Experiments conducted using the Infrared Kinetic Spectroscopy (IRKS) apparatus to
29
30 study peroxy radical chemistry have been reported in earlier publications.³¹⁻³³ Therefore, the
31
32 method is discussed only briefly here with an emphasis on improvements in the detection
33
34 capabilities and details specific to this work. The general schematic is shown in Figure 2.
35
36
37
38
39
40
41
42
43
44
45
46
47
48
49
50
51
52
53
54
55
56
57
58
59
60

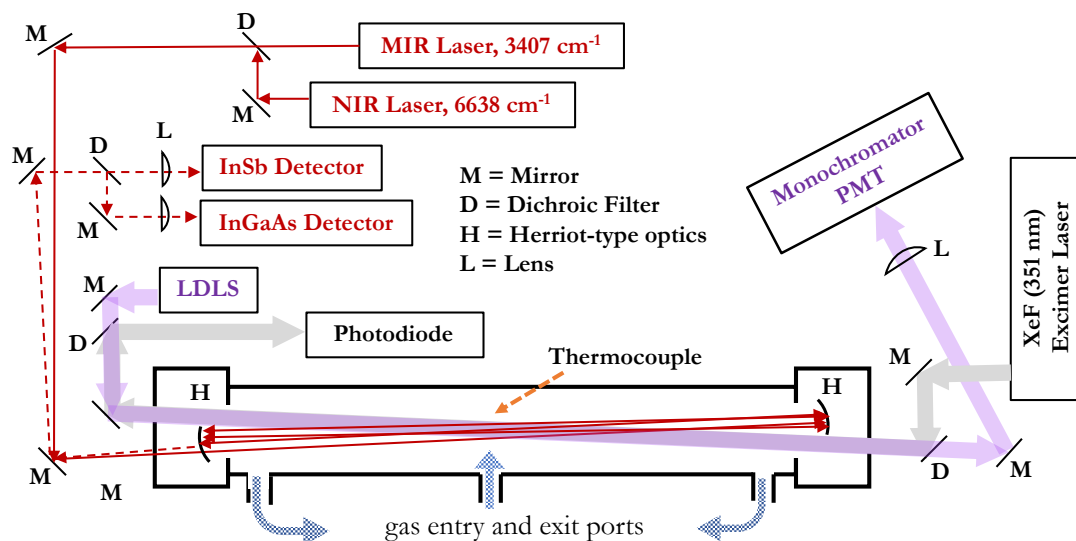


Figure 2. Experimental schematic of the IRKS apparatus. M, D, H, and L are mirrors, dichroic filters, half-moon shaped Herriott mirrors, and lenses, respectively. The Herriott mirrors are housed inside nitrogen purged boxes attached to the jacketed cell. Solid Red lines represent the IR beam paths prior to entering the cell, the reflecting red lines in the cell represent thirty passes in a Herriott optic geometry, and the dashed red lines represent the IR beam paths after exiting the cell. The laser driven UV light source (LDLS) and 351 nm photolysis laser counter-propagated the cell entering/exiting the cell at a height offset but crossing the IR beam paths.

Pulsed laser photolysis (PLP) by a XeF excimer laser (Lambda Physik Compex 301, 351 nm, 110 mJ/pulse in constant energy mode, 0.2 Hz repetition rate) was used to initiate reactions in a continuous, temperature-controlled ($T = 298 \pm 1$ K) flow cell (175 cm long, 5 cm diameter). The repetition rate of the photolysis laser was set to ensure products diffused out of the reaction volume between pulses and the flow cell pressure and temperature were held constant at 100 Torr and 298 K, respectively. Collimated broadband UV light generated by a laser driven light source (LDLS, Energetiq EQ-99XFC) counter propagated the excimer beam path through the cell and was separated from the excimer beam by a dichroic mirror and dispersed using a monochromator (Acton Research Corporation Spectra Pro-300i, slit width ~ 160 μm) coupled to a photomultiplier tube (EMI 9781A) for UV absorption measurements. The gas exit port positions (located in front of the Herriott mirrors, as shown in Figure 2) dictated the UV absorption

1
2
3 pathlength, which was measured to be 148 ± 10 cm long by Cl_2 absorption at 320 nm ($\sigma_{\text{Cl}_2} =$
4
5 $2.37 \times 10^{-19} \text{ cm}^2$).³¹
6
7

8 Two continuous-wave distributed feedback IR lasers (NASA JPL Microdevices
9 Laboratory), were each wavelength modulated at 6.8 MHz, entered the cell through a hole in a
10 custom coated mirror (Rocky Mountain Instrument Co.) aligned in a Herriott optical
11 arrangement to achieve thirty passes through the cell, resulting in a total IR effective path length
12 of approximately 27 m for each laser.³⁴ The Herriott mirrors were mounted inside nitrogen
13 purged boxes attached to both ends of the cell as shown in Figure 2. After exiting the cell, the IR
14 signals were detected independently using an indium gallium arsenide detector (InGaAs, New
15 Focus 1811) and a liquid nitrogen-cooled indium antimonide detector (InSb, Infrared Associates
16 IS-0.25) for the near- and mid-IR light, respectively. These signals were demodulated at 13.6
17 MHz and amplified by a factor of 200 for $2f$ -heterodyne detection. Similar to previous works,³¹⁻³³
18 the concentrations derived from the $2f$ signals for both lasers detection axes were calibrated daily
19 (See SI for details.).
20
21
22
23
24
25
26
27
28
29
30
31
32
33
34

35 In a typical experiment, the time-dependent UV absorption trace and the two IR kinetic
36 traces were recorded simultaneously following the excimer photolysis pulse. Typical datasets
37 comprised all three signals that were digitized and averaged for 800 excimer shots while
38 simultaneously being recorded using NI LabVIEW software.
39
40
41
42
43
44

45 **Chemicals and Radical Generation**

46 Measured flows of nitrogen carrier gas (N_2 , Airgas Corps., 99.997%) were bubbled
47 through methanol (CH_3OH , Fisher Optima A454-1, >99.9%) and acetone ($\text{CH}_3\text{C}(\text{O})\text{CH}_3$, Fisher
48 Optima A929-1, >99.9%) to entrain these species in the gas phase. Changes in the bubbler flow
49 rates were used to vary the concentrations of gaseous CH_3OH and $\text{CH}_3\text{C}(\text{O})\text{CH}_3$. These
50
51
52
53
54
55
56
57
58
59
60

precursor gases were combined and premixed in a temperature-controlled glass manifold with chlorine (Cl₂, Air Products, 9.99% in He), oxygen (O₂, Airgas Corps., 99.996%), and N₂ (Airgas Corps., 99.997%) and then introduced through a central port of the flow cell (at the same temperature) depicted in Figure 2. Individual flow rates of the reaction precursors and the nitrogen bath gas were controlled using mass flow controllers (MKS Instruments). The total flow rate was 2160 sccm and the flow cell residence time was 9.7 s.

Photolysis of Cl₂ by pulsed 351 nm light generated atomic chlorine, Cl, to initiate reactions with CH₃C(O)CH₃ (R4) and CH₃OH (R6) to generate CH₃C(O)CH₂O₂ (R5) and HO₂ (R7), respectively, in the presence of O₂.



Typical initial concentrations for investigating the cross-reaction, R1, averaged [Cl₂] = 9 – 10 × 10¹⁵, [Cl]₀ = 1 – 2 × 10¹⁴, [CH₃OH] = 4 × 10¹⁵, [CH₃C(O)CH₃] = 1.7 – 2.8 × 10¹⁶, and [O₂] = 1.6 × 10¹⁸ molecule cm⁻³ with N₂ added to achieve the total pressure. Concentrations of the precursors for observing R1 were set to have ratios of [HO₂]/[CH₃C(O)CH₂O₂] between 4 – 6 to keep HO₂ in excess of CH₃C(O)CH₂O₂ to reduce secondary chemistry from the CH₃C(O)CH₂O₂ self-reaction. Similar initial concentrations in the absence of CH₃OH were used for the UV cross-section measurements and for investigating R2.

Detection of Key Species

Combining the UV absorption and IR-WMS techniques makes this the first study to simultaneously monitor the time-dependent concentrations of CH₃C(O)CH₂O₂, HO₂, and OH

1
2
3 radicals. $\text{CH}_3\text{C}(\text{O})\text{CH}_2\text{O}_2$ concentrations were detected by UV absorption spectroscopy using 312
4
5 nm light. At the same time, IR-WMS was used to monitor concentrations of HO_2 and the product
6
7 OH at 6638.2 and 3407.6 cm^{-1} , respectively, via ro-vibrational lines. Under these experimental
8
9 conditions, the normalized noise-equivalent sensitivity concentrations for the detection of HO_2
10
11 and OH radicals were on the order of $10^8 \text{ molecule cm}^{-3} \text{ Hz}^{-1/2}$ ($10^9 \text{ molecule cm}^{-3}$ for typical
12
13 experiments).
14
15

16 17 **Iib. Kinetic Modeling for Fitting Experimental Data**

18
19 Because of the large number of reactions involved, numerical chemical simulations were
20
21 necessary for extracting quantitative results for the rate constants and branching fractions of R1
22
23 and R2. A Python code adapted from an existing library³⁵ was used as a numerical integrator and
24
25 fitting software encompassing the comprehensive mechanism shown in Table 1. The reaction list
26
27 was constructed from a combination of the reactions listed in the JPL Data Evaluation 15-10 and
28
29 relevant papers.^{18, 33, 36} $\text{CH}_3\text{C}(\text{O})\text{CH}_2\text{O}_2$, HO_2 , and OH kinetic data were fit simultaneously using
30
31 a Levenberg-Marquardt algorithm^{37, 38} to optimize the kinetic rate constants and branching
32
33 fractions against the datasets. Weights were applied to equalize the fitting across the different
34
35 magnitudes of species concentrations. The fits were iterated 1000 times per experimental run
36
37 following a Monte Carlo (MC) algorithm to randomly sample all parameters and systematic
38
39 uncertainties (reaction rate constants and branching fractions, concentrations, calibration
40
41 constants, the cell pathlength, Poisson counting in the data, and absorption cross sections) within
42
43 each respective uncertainty. Initial guesses for the fitted parameters were sampled manually to
44
45 ensure local minima were avoided. This procedure resulted in distributions of each fitted
46
47 parameter from which its mean and uncertainty (reported as 1σ unless otherwise stated) could
48
49 then be determined.
50
51
52
53
54
55
56
57
58
59
60

The self-reaction data (R2) was analyzed first. Here, OH and HO₂ kinetics are the result of secondary chemistry that is directly affected by the overall kinetic rate of R2 and the branching fraction R2b/R2 (discussed in section IIIb). The resulting fits determined the overall rate constant k_2 and the branching fraction, k_{2b}/k_2 . In order to determine the rate constant and branching fraction for the cross-reaction, R1, the results of fitting R2 were incorporated into the model, and the experimental concentrations were set to minimize contributions from R2 by keeping HO₂ in excess of CH₃C(O)CH₂O₂ ($[\text{HO}_2]/[\text{CH}_3\text{C}(\text{O})\text{CH}_2\text{O}_2] > 4$). The sensitivity of the model for the cross-reaction to the rate of the self-reaction was tested and found to be negligible for the range $k_2 = 3.5 - 6.0 \times 10^{-12} \text{ cm}^3 \text{ molecule}^{-1} \text{ s}^{-1}$ under the conditions used in this work. The three [CH₃C(O)CH₂O₂], [HO₂] and [OH] time-dependent datasets were again fit simultaneously. For experimental runs of R1, the fitted parameters included k_{1a} , k_{1b} , and the chaperone enhanced HO₂ self-reaction rate constant, $k_{12,\text{obs}}$ (sections IIIb and IIIc). Following the determination of the fit parameters for the cross-reaction, these values were used to re-run the MC simulations for the self-reaction data to verify that the final values of k_2 and k_{2b}/k_2 were unaffected by the change in k_{1a} , k_{1b} , and $k_{12,\text{obs}}$.

Table 1. Reaction scheme used in the determination of rates, branching fractions, and chaperone effects for the self- and cross- reactions of CH₃C(O)CH₂O₂ and HO₂. Rate constants are taken from the JPL Data Evaluation 15-10 recommended values³⁶ and are all in cm³ molecule⁻¹ s⁻¹, unless indicated otherwise. Uncertainties in values are given in their respective references.

k	Reaction	Branching Ratio	Rate Constant	Ref.
Initial Radical Reactant Generation				
k_6	CH ₃ OH + Cl → CH ₂ OH + HCl		5.5×10^{-11}	
k_7	CH ₂ OH + O ₂ → HO ₂ + CH ₂ O		9.1×10^{-12}	
k_4	CH ₃ C(O)CH ₃ + Cl → CH ₃ C(O)CH ₂ + HCl		$1.63 \times 10^{-11} \exp(-610/T)$	
k_{5a}	CH ₃ C(O)CH ₂ + O ₂ (+M) → CH ₃ C(O)CH ₂ O ₂	0.98	$2.75 \times 10^{-31}[\text{M}]$	
k_{5b}	CH ₃ C(O)CH ₂ + O ₂ (+M) → OH + products	0.01		
k_{5c}	CH ₃ C(O)CH ₂ + O ₂ (+M) → HO ₂ + products	0.01		

Primary Chemistry				
k_{12}	$\text{HO}_2 + \text{HO}_2 \rightarrow \text{H}_2\text{O}_2 + \text{O}_2$		$1.5 \times 10^{-12} + 4.0 \times 10^{-29} \times [\text{CH}_3\text{C}(\text{O})\text{CH}_3]$	<i>this work</i>
k_{2a}	$2\text{CH}_3\text{C}(\text{O})\text{CH}_2\text{O}_2 \rightarrow \text{CH}_3\text{C}(\text{O})\text{CHO} + \text{CH}_3\text{C}(\text{O})\text{CH}_2\text{OH} + \text{O}_2$		4.8×10^{-12}	<i>this work</i>
k_{2b}	$2\text{CH}_3\text{C}(\text{O})\text{CH}_2\text{O}_2 \rightarrow 2 \text{CH}_3\text{C}(\text{O})\text{CH}_2\text{O} + \text{O}_2$	0.68		
k_{2c}	$2\text{CH}_3\text{C}(\text{O})\text{CH}_2\text{O}_2 \rightarrow \text{accretion products}$			
k_{1a}	$\text{HO}_2 + \text{CH}_3\text{C}(\text{O})\text{CH}_2\text{O}_2 \rightarrow \text{CH}_3\text{C}(\text{O})\text{CH}_2\text{OOH} + \text{O}_2$	0.70	5.5×10^{-12}	<i>this work</i>
k_{1b}	$\text{HO}_2 + \text{CH}_3\text{C}(\text{O})\text{CH}_2\text{O}_2 \rightarrow \text{CH}_3\text{C}(\text{O})\text{CH}_2\text{O} + \text{OH} + \text{O}_2$	0.30		<i>this work</i>
Secondary Chemistry				
	$\text{OH} + \text{CH}_3\text{OH} \rightarrow \text{CH}_2\text{OH} + \text{H}_2\text{O}$	0.85	$2.9 \times 10^{-12} \exp(-345/T)$	
	$\text{OH} + \text{CH}_3\text{OH} \rightarrow \text{CH}_3\text{O} + \text{H}_2\text{O}$	0.15		
	$\text{OH} + \text{CH}_3\text{C}(\text{O})\text{CH}_3 \rightarrow \text{H}_2\text{O} + \text{CH}_3\text{COCH}_2$	0.98	$1.33 \times 10^{-13} + 3.82 \times 10^{-11} \times \exp(-2000/T)$	
	$\text{OH} + \text{CH}_3\text{C}(\text{O})\text{CH}_3 \rightarrow \text{CH}_3 + \text{CH}_3\text{COOH}$	0.02		
k_{11}	$\text{Cl} + \text{HO}_2 \rightarrow \text{OH} + \text{ClO}$		$3.6 \times 10^{-11} \exp(-375/T)$	
	$\text{Cl} + \text{HO}_2 \rightarrow \text{O}_2 + \text{HCl}$		$1.4 \times 10^{-11} \exp(270/T)$	
	$2 \text{CH}_3\text{O}_2 \rightarrow 2 \text{CH}_3\text{O} + \text{O}_2$	0.59	3.5×10^{-13}	
	$2 \text{CH}_3\text{O}_2 \rightarrow \text{CH}_3\text{OH} + \text{CH}_2\text{O} + \text{O}_2$	0.41		
	$\text{HO}_2 + \text{CH}_3\text{O}_2 \rightarrow \text{CH}_3\text{OOH} + \text{O}_2$	0.9	5.2×10^{-12}	
	$\text{HO}_2 + \text{CH}_3\text{O}_2 \rightarrow \text{CH}_2\text{O} + \text{H}_2\text{O} + \text{O}_2$	0.1		
	$\text{OH} + \text{CH}_3\text{OOH} \rightarrow \text{products}$		$3.8 \times 10^{-12} \exp(200/T)$	
	$\text{CH}_3\text{O} + \text{O}_2 \rightarrow \text{CH}_2\text{O} + \text{HO}_2$		$3.9 \times 10^{-14} \exp(-900/T)$	
	$\text{O} + \text{CH}_2\text{O} \rightarrow \text{products}$		$3.4 \times 10^{-11} \exp(-1600/T)$	
	$\text{OH} + \text{CH}_2\text{O} \rightarrow \text{H}_2\text{O} + \text{HCO}$		$5.5 \times 10^{-12} \exp(125/T)$	
	$\text{HO}_2 + \text{CH}_2\text{O} \rightarrow \text{HOCH}_2\text{O}_2$		$6.7 \times 10^{-15} \exp(600/T)$	
	$\text{CH}_3 + \text{O}_2 (+\text{M}) \rightarrow \text{CH}_3\text{O}_2$		$1.16 \times 10^{-31} [\text{M}]$	
	$\text{CH}_3\text{O}_2 + \text{CH}_3\text{C}(\text{O})\text{CH}_2\text{O}_2 \rightarrow \text{CH}_3\text{C}(\text{O})\text{CH}_2\text{O} + \text{CH}_3\text{O} + \text{O}_2$	0.3	$7.5 \times 10^{-13} \exp(500/T)$	
	$\text{CH}_3\text{O}_2 + \text{CH}_3\text{C}(\text{O})\text{CH}_2\text{O}_2 \rightarrow \text{CH}_3\text{C}(\text{O})\text{CH}_2\text{OH} + \text{CH}_2\text{O} + \text{O}_2$	0.2		
	$\text{CH}_3\text{O}_2 + \text{CH}_3\text{C}(\text{O})\text{CH}_2\text{O}_2 \rightarrow \text{CH}_3\text{C}(\text{O})\text{CHO} + \text{CH}_3\text{OH} + \text{O}_2$	0.5		
k_{10}	$\text{CH}_3\text{C}(\text{O})\text{CH}_2\text{O} + \text{O}_2 \rightarrow \text{CH}_3\text{C}(\text{O})\text{CHO} + \text{HO}_2$		9.7×10^{-15}	39
k_8	$\text{CH}_3\text{C}(\text{O})\text{CH}_2\text{O} \rightarrow \text{CH}_3\text{CO} + \text{CH}_2\text{O}$		rapid	39
	$\text{OH} + \text{HO}_2 \rightarrow \text{H}_2\text{O} + \text{O}_2$		$4.8 \times 10^{-11} \exp(250/T)$	
	$\text{O} + \text{O}_2 (+\text{M}) \rightarrow \text{O}_3$		$6.10 \times 10^{-24} [\text{M}]$	
	$\text{OH} + \text{HCl} \rightarrow \text{H}_2\text{O} + \text{Cl}$		$1.8 \times 10^{-12} \exp(-250/T)$	
k_{9a}	$\text{CH}_3\text{CO} + \text{O}_2 (+\text{M}) \rightarrow \text{CH}_3\text{C}(\text{O})\text{O}_2$	0.97	3.99×10^{-12}	40

1					
2					
3	k_{9b}	$\text{CH}_3\text{CO} + \text{O}_2 \rightarrow \text{OH} + \text{products}$	0.01		
4	k_{9c}	$\text{CH}_3\text{CO} + \text{O}_2 \rightarrow \text{HO}_2 + \text{products}$.02		
5					
6		$\text{HO}_2 + \text{CH}_3\text{C}(\text{O})\text{O}_2 \rightarrow \text{CH}_3\text{C}(\text{O})\text{OOH} + \text{O}_2$	0.29	1.72×10^{-11}	33
7					
8		$\text{HO}_2 + \text{CH}_3\text{C}(\text{O})\text{O}_2 \rightarrow \text{CH}_3\text{C}(\text{O})\text{OH} + \text{O}_3$	0.23		
9					
10		$\text{HO}_2 + \text{CH}_3\text{C}(\text{O})\text{O}_2 \rightarrow \text{OH} + \text{CH}_3\text{CO}_2 + \text{O}_2$	0.48		
11					
12		$\text{CH}_3\text{O}_2 + \text{CH}_3\text{C}(\text{O})\text{O}_2 \rightarrow \text{CH}_3\text{CO}_2 + \text{CH}_3\text{O} + \text{O}_2$	0.9	$2.0 \times 10^{-12} \exp(500/T)$	
13					
14		$\text{CH}_3\text{O}_2 + \text{CH}_3\text{C}(\text{O})\text{O}_2 \rightarrow \text{CH}_3\text{C}(\text{O})\text{OH} + \text{CH}_2\text{O} + \text{O}_2$	0.1		
15					
16		$\text{CH}_3\text{CO}_2 \rightarrow \text{CH}_3 + \text{CO}_2$		rapid	39
17					
18		$\text{CH}_3\text{C}(\text{O})\text{CH}_2\text{O}_2 + \text{CH}_3\text{C}(\text{O})\text{O}_2 \rightarrow \text{CH}_3\text{C}(\text{O})\text{CH}_2\text{O} + \text{CH}_3\text{CO}_2 + \text{O}_2$	0.5	5.0×10^{-12}	21,41
19					
20		$\text{CH}_3\text{C}(\text{O})\text{CH}_2\text{O}_2 + \text{CH}_3\text{C}(\text{O})\text{O}_2 \rightarrow \text{CH}_3\text{C}(\text{O})\text{CHO} + \text{CH}_3\text{C}(\text{O})\text{OH} + \text{O}_2$	0.5		
21					
22		$2 \text{CH}_3\text{C}(\text{O})\text{O}_2 \rightarrow \text{CH}_3\text{CO}_2 + \text{O}_2 + \text{CH}_3\text{CO}_2$		$2.9 \times 10^{-12} \exp(500/T)$	
23					
24		$\text{HOCH}_2\text{O}_2 + \text{HO}_2 \rightarrow \text{OH} + \text{O}_2 + \text{HOCH}_2\text{O}$		$5.6 \times 10^{-15} \exp(2300/T)$	42, 43

IIc. THEORETICAL METHODS AND ENERGETICS

The potential for OH recycling via unimolecular reactions following O_2 -addition to the acetyl radical was modelled using a Rice-Ramsperger-Kassel-Marcus (RRKM) master equation (ME) approach reflecting the experimental conditions. The energetics are calculated as described in the approach by Møller et al.⁴⁴ and briefly outlined here. Conformers of reactants, transition states (TSs) and products are sampled using MMFF in Spartan '18 based on optimized structures at the B3LYP/6-31+G(d) level from Gaussian 16, rev. C.01.⁴⁵⁻⁵² For the transition states, suitable bond lengths are constrained in the conformer sampling. The resulting conformers are optimized at the B3LYP/6-31+G(d) level in Gaussian 16.⁵⁰ Unique conformers^{44, 53} within 2 kcal mol⁻¹ in electronic energy of the lowest energy conformer are further optimized at the ω B97X-D/aug-cc-pVTZ level⁵⁴⁻⁵⁷ in Gaussian 16. For the conformer lowest in zero-point corrected electronic energy at this level, an RO-CCSD(T)-F12a/VDZ-F12 single-point calculation is done in Molpro2012.⁵⁸⁻⁶³ The reactions are modelled using the Master Equation Solver for Multi Energy-well Reactions (MESMER)⁶³ based on the ω B97X-D/aug-cc-pVTZ thermodynamic properties of the lowest-energy conformers and improved using the RO-

1
2
3 CCSD(T)-F12a/VDZ-F12// ω B97X-D/aug-cc-pVTZ electronic energies. Further details of the
4
5 MESMER modelling are given in the Supplemental Information (SI) Section SII. The rate
6
7 coefficients for the unimolecular reactions of the thermalized species modelled are further
8
9 calculated using the multi-conformer transition state theory (MC-TST) approach by Møller et
10
11 al.⁴⁴ including the Eckart tunneling correction.⁶⁴ Rate coefficients of additional possible
12
13 unimolecular reactions from subsequent intermediates were calculated at the same level of theory
14
15 to aid the analysis of the experimental results (Section SIII in SI). All calculations are done at
16
17 298.15K.
18
19
20

21 III. RESULTS

22 IIIa. CH₃C(O)CH₂O₂ UV Absorption Cross-Section

23
24
25
26 The inset in Figure 3 displays a typical set of UV absorption data used to assess
27
28 $\sigma_{\text{CH}_3\text{C}(\text{O})\text{CH}_2\text{O}_2}$ in the spectral region $\lambda = 290 - 320$ nm for select wavelengths (see SV in SI for
29
30 complete data set). Experimental parameters were held constant as the monochromator grating
31
32 position scanned across the spectral window in 5 nm steps. CH₃C(O)CH₂O₂ is a transient
33
34 species, therefore, the reaction kinetics are coupled to quantifying $\sigma_{\text{CH}_3\text{C}(\text{O})\text{CH}_2\text{O}_2}$. Kinetic
35
36 modeling was used to determine the time window for applying the fit at early times (0 – 2 ms)
37
38 representative of second-order kinetics. The time window for the fit was optimized to exclude (1)
39
40 scattered light and fluorescence from the excimer pulse which saturates the probe beam detector
41
42 at early times ($t < 0.2$ ms), and (2) the influence of absorption from secondary species that absorb
43
44 in this spectral region at later times (see SIV in SI for details). The inverse absorbance, 1/Abs,
45
46 vs. time was used under the assumption of second-order analysis in this time range. The
47
48 integrated rate law for second-order kinetics dictates that a linear fit corresponds to Equation 1
49
50
51
52
53

$$54 \frac{1}{Abs} = \frac{2k_2t}{\sigma_{\text{CH}_3\text{C}(\text{O})\text{CH}_2\text{O}_2}l} + \frac{1}{[\text{CH}_3\text{C}(\text{O})\text{CH}_2\text{O}_2]_0\sigma_{\text{CH}_3\text{C}(\text{O})\text{CH}_2\text{O}_2}l} \quad [E1]$$

55
56
57
58
59
60

where l is the pathlength of the absorption measurement, k_2 is the bimolecular rate constant for R2, and $[\text{CH}_3\text{C}(\text{O})\text{CH}_2\text{O}_2]_0$ is the initial concentration of $\text{CH}_3\text{C}(\text{O})\text{CH}_2\text{O}_2$ formed at $t = 0$ s following reaction of the radical precursors. $[\text{CH}_3\text{C}(\text{O})\text{CH}_2\text{O}_2]_0$ was equated with $[\text{Cl}]_0$ determined during the calibration experiments (see SI for details). In the absence of CH_3OH to form HO_2 , the same initial concentration of $\text{CH}_3\text{C}(\text{O})\text{CH}_2\text{O}_2$ forms under the condition of constant excimer power and $[\text{Cl}]_0$. The y-intercept from the linear fit was used to calculate the value of $\sigma_{\text{CH}_3\text{C}(\text{O})\text{CH}_2\text{O}_2}$ using E1. Our results are shown in Table 2 and Figure 4 with comparison to prior studies.^{21, 26, 29, 36} The reported uncertainties were calculated through propagation of error and include the uncertainty in the linear fit, the pathlength, and the determined initial concentrations.

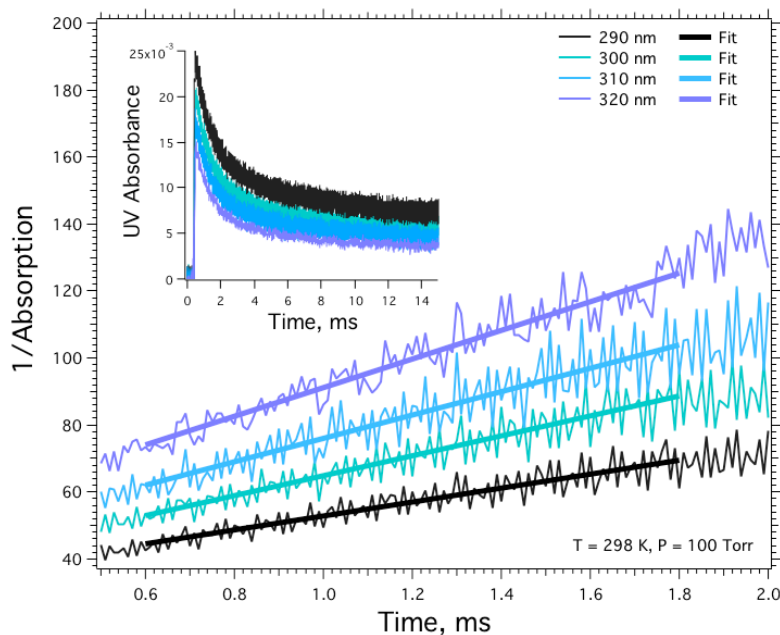


Figure 3. UV $1/\text{Abs}$ vs. time measurements obtained for $\text{CH}_3\text{C}(\text{O})\text{CH}_3/\text{Cl}_2/\text{O}_2/\text{N}_2$ mixtures under conditions of constant laser power and $[\text{Cl}_2]$ to observe the $\text{CH}_3\text{C}(\text{O})\text{CH}_2\text{O}_2$ self-reaction. Each UV time trace shown in the inset for selected wavelengths in the range $\lambda = 290 - 320$ nm was converted to $1/\text{Abs}$ and fit with a linear regression following second order kinetics in the $0.6 - 2$ ms range. Additional datasets are shown in Figure S8 in the SI.

Table 2: Absorption cross-sections of $\text{CH}_3\text{C}(\text{O})\text{CH}_2\text{O}_2$, $\sigma_{\text{CH}_3\text{C}(\text{O})\text{CH}_2\text{O}_2}$, measured at $T = 298 (\pm 1)$ K and $P = 100 (\pm 1)$ Torr. Propagation of error for the reported uncertainties accounts for the uncertainties in the fits, pathlength, and initial radical concentrations.

λ (nm)	$10^{20} \sigma$ ($\text{cm}^2 \text{ molecule}^{-1}$)
290	212 (± 38)
295	196 (± 32)
300	192 (± 31)
305	166 (± 23)
310	164 (± 22)
315	163 (± 22)
320	141 (± 17)

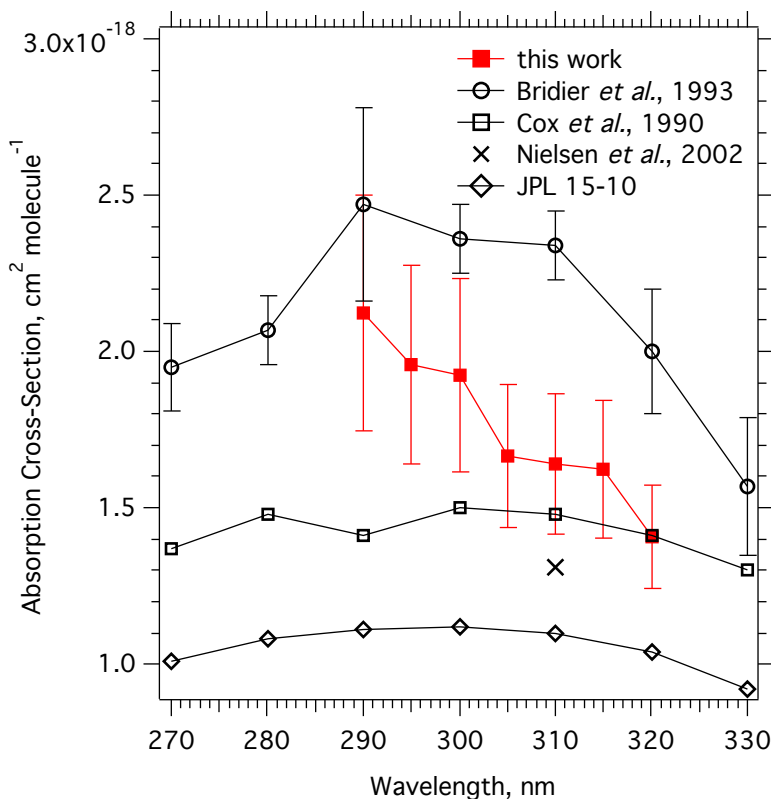


Figure 4. Comparison of the $\text{CH}_3\text{C}(\text{O})\text{CH}_2\text{O}_2$ cross-section, $\sigma_{\text{CH}_3\text{C}(\text{O})\text{CH}_2\text{O}_2}$, measured from this work (red squares), Bridier *et al.* (circles),²¹ Cox *et al.* (squares),²⁶ Nielsen *et al.* (\times),²⁹ and the recommended values by JPL Evaluation 15-10 (diamonds)³⁵ which reports the cross-section values from Cox *et al.* re-normalized to the absolute value at 240 nm measured by Nielsen *et al.* Errors in literature cross-section values were not available for all of the previous works as shown.

IIIb. $\text{CH}_3\text{C}(\text{O})\text{CH}_2\text{O}_2$ self-reaction kinetics

Figure 5 shows comparisons between experimental data and the kinetic model using the IUPAC⁶⁶ recommended value of k_2 , $8.0 \times 10^{-12} \text{ cm}^3 \text{ molecule}^{-1} \text{ s}^{-1}$, vs. the value for k_2 determined from our MC simulations, $4.8 \times 10^{-12} \text{ cm}^3 \text{ molecule}^{-1} \text{ s}^{-1}$. As is clearly seen, the recommended value for k_2 does not capture the $\text{CH}_3\text{C}(\text{O})\text{CH}_2\text{O}_2$ kinetics observed in our experiments. Although Equation 1 could be used to determine the effective rate constant for R2 using the slope of the linear fit, it would result in large experimental uncertainty as a result of fitting only over a narrow temporal window. Fitting only $\text{CH}_3\text{C}(\text{O})\text{CH}_2\text{O}_2$ would also leave determination of k_2 less constrained. To overcome these deficiencies, the concentration time profiles of HO_2 and OH were fit simultaneously with the $\text{CH}_3\text{C}(\text{O})\text{CH}_2\text{O}_2$ radical kinetics using the MC simulation fitting method and model mechanism described in Section IIb and the absorption cross-sections given in Table 2. The time windows for the fits were 0.6 – 4, 0 – 20, and 0 – 2 ms for the $\text{CH}_3\text{C}(\text{O})\text{CH}_2\text{O}_2$, HO_2 , and OH kinetic traces, respectively, in order to disregard the early times for the UV data (<0.2 ms) that are affected by the excimer laser and data from later times to minimize higher contributions from secondary chemistry for each species.

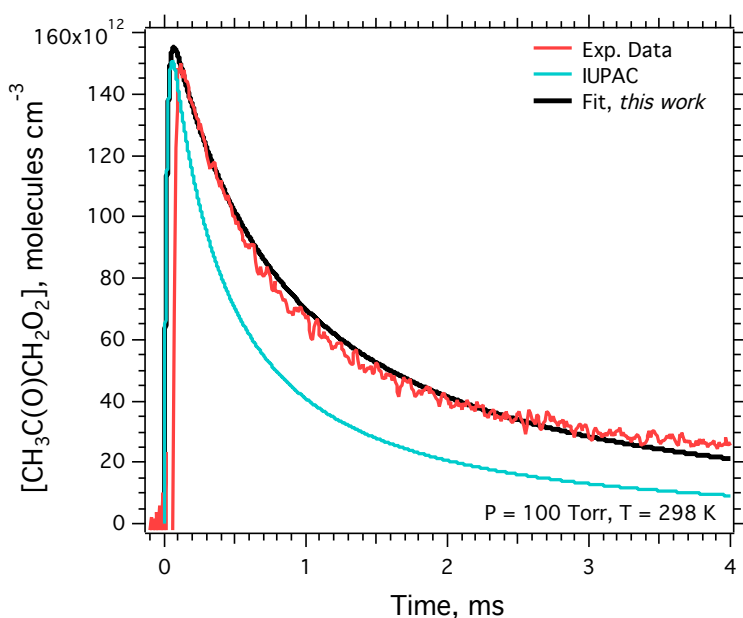


Figure 5. Experimental data (red) for $[\text{CH}_3\text{C}(\text{O})\text{CH}_2\text{O}_2]$ vs. time obtained by UV absorption measurements at 312 nm using linear interpolation of the 310 and 315 nm UV cross-sections determined in this work (Table 2). The kinetic simulation generated with recommended rate parameters for k_2 and k_{2b}/k_2 by IUPAC⁶⁶ is shown in turquoise and the fit from the MC simulations is shown in black.

Figure 6a and 6b show the experimental vs. simulated time-dependent HO_2 and OH concentrations, respectively, where the simulated kinetic profiles for each species using the IUPAC recommended values⁶⁶ are shown in turquoise. Results of this work, where k_2 and k_{2b}/k_2 were fit to the experimental data, are shown in black in Figure 6 and histograms representing the occurrences for the k_2 and k_{2b}/k_2 parameters from the MC simulations are shown in Figure 7. The magnitudes of both the OH and HO_2 simulated kinetic concentrations, shown in Figure 6, were extremely sensitive to the branching fraction for $\text{CH}_3\text{C}(\text{O})\text{CH}_2\text{O}$ formation, R2b, in the mechanism. The use of the IUPAC recommended value⁶⁶ for the branching fraction, $k_{2b}/k_2 = 0.63 (\pm 0.20)$, overpredicted our experimental observations for the HO_2 and OH concentrations by a factor of ~ 2 . Fitting the experimental data yielded a branching fraction of $k_{2b}/k_2 = 0.33 (\pm 0.13)$ and dramatically reduced the discrepancies between the kinetic model and our data.

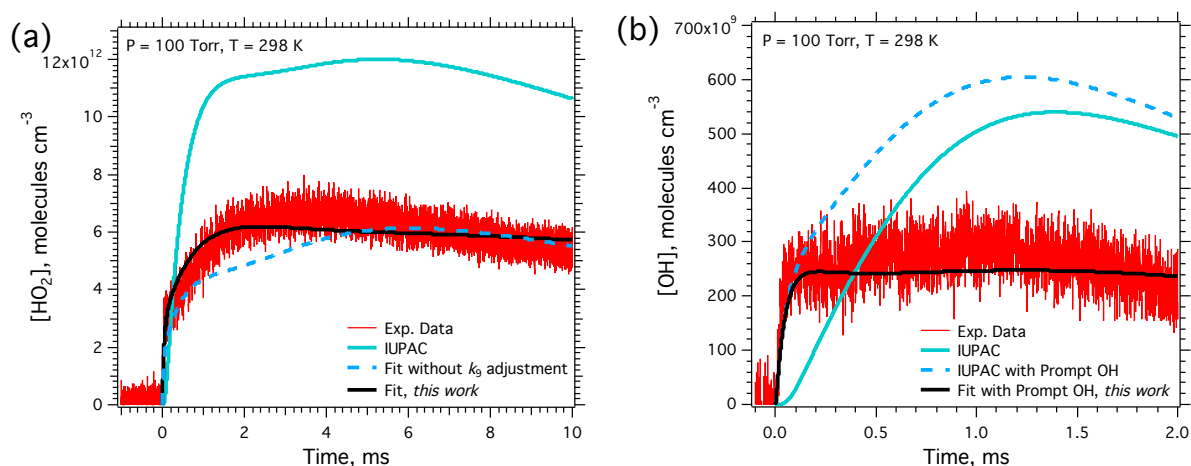


Figure 6. Experimental (red) and calculated kinetic profiles for (a) HO_2 and (b) OH for the $\text{CH}_3\text{C}(\text{O})\text{CH}_2\text{O}_2$ self-reaction. The kinetic model (turquoise) shows the simulated concentrations using the IUPAC recommended rate parameters⁶⁶ and the results of the fit (black) shows the simulated concentrations with the parameters from this work. The dashed blue lines show (a) the fit without k_9 adjustment (see text) and (b) the model simulated with prompt OH arising from the acetyl + O_2 reaction (see text) for comparison. The uncertainties in the experimentally

measured HO₂ and OH concentrations were $\pm 3.2 \times 10^{10}$ and $\pm 1.4 \times 10^9$ molecules cm⁻³, respectively.

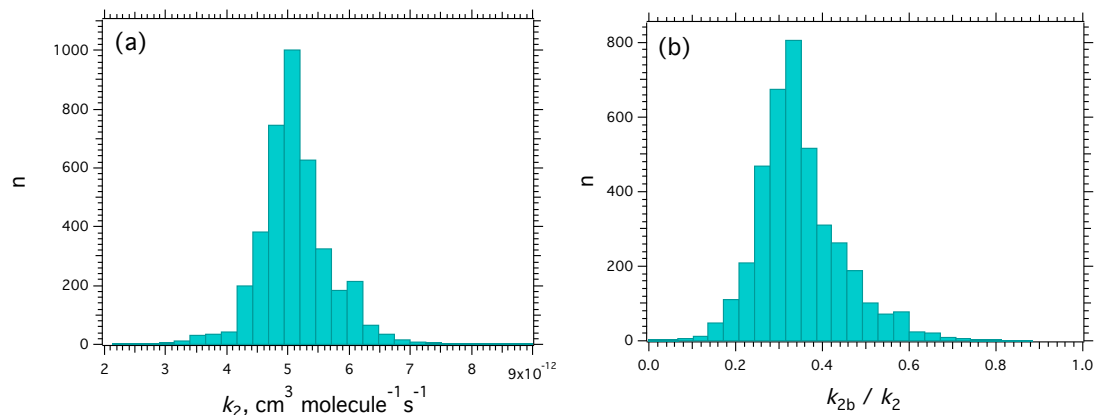


Figure 7. Histogram output from the MC simulations (4000 iterations) for (a) $k_2 = (4.8 \pm 0.8) \times 10^{-12} \text{ cm}^3 \text{ molecule}^{-1} \text{ s}^{-1}$ and (b) $k_{2b} / k_2 = 0.33 \pm 0.13$.

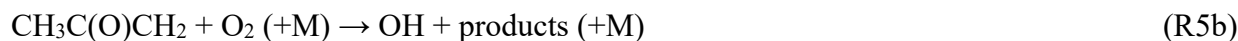
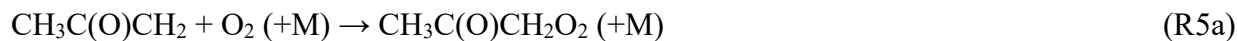
The fit in Figure 5 was primarily dependent on the absolute concentration of the CH₃C(O)CH₂O product formation through the R2b channel as opposed to the relative product formation between R2b and the other reaction pathways as discussed in Section IIIa. Equivalent fits to that shown in Figure 6 were achieved when maintaining a branching fraction for R2b pathway of 0.33 (± 0.13) with any combined remaining branching fraction of the R2a + R2c. Therefore, our experiments cannot distinguish between the other two channels, R2a and R2c. However, the recent mass-spectrometry study by Berndt et al.²⁸ observed and proposed a mechanism for a third channel, R2c, for the CH₃C(O)CH₂O₂ self-reaction which leads to accretion product formation (ROOR) with a rate constant of $1.3 \times 10^{-12} \text{ cm}^3 \text{ molecule}^{-1} \text{ s}^{-1}$. Their results inferred a product branching fraction at 295 K for R2c of 0.16 based on the recommended overall k_2 . Based on their rate constant for R2c and k_2 determined in this work, a larger branching fraction for the R2c accretion product channel of 0.30 was calculated.

Monitoring the HO₂ and OH concentrations constrained the fit for the rate constant and branching fractions while also providing insight to the secondary chemistry arising from R2. The secondary chemistry is complex; however, the difference in the chemical timescales for the

modeled reaction mechanism in comparison to the experimental data enabled the characterization of the experimentally observed HO₂ and OH concentrations. A possible explanation for the relationship between the time-dependent HO₂ and OH concentrations and the magnitude of the branching fraction involve the subsequent alkoxy product chemistry. Here, the CH₃C(O)CH₂O product formation rapidly decomposes to the acetyl, CH₃CO, product (R8) which is oxidized to form acetyl peroxy, CH₃C(O)O₂ (R9a), OH (R9b) and HO₂ (R9c).³⁹



To achieve the calculated kinetic profiles for the fits shown in Figure 6, two rate parameters had to be adjusted relative to the recommended values shown in Table 1 in addition to fitting the overall CH₃C(O)CH₂O₂ self-reaction kinetic parameters. First, there was a significant absence of prompt OH being formed in the calculated model at early times (<0.2 ms). Augmenting the oxygenation reaction of the alkyl group (acetyl, CH₃C(O)CH₂) in the initial formation of CH₃C(O)CH₂O₂ to include 0.02 ± 0.01 product OH formation (R5b) affected the calculated model as shown by the dashed blue line in Figure 6b.



The mechanism for the proposed OH formation is not resolved and further discussion of the validity of this alkyl chemistry is discussed in section IV. Due to the timescale of the prompt OH, the inclusion of prompt OH formation mechanism did not affect the fit for the branching

1
2
3 fraction, k_{2b} / k_2 . The second parameter that was adjusted was the rate constant k_9 corresponding
4
5 to reaction between $\text{CH}_3\text{C}(\text{O})\text{CH}_2\text{O}$ and O_2 (R10).



9
10 This reaction was shown to affect the calculated HO_2 concentrations on the time scales between 0
11
12 – 5 ms, as shown in Figure 6a (dashed blue). Increasing the rate constant by a factor of two
13
14 greatly improved the fit to the experimental data. As this rate constant is relatively small
15
16 compared to the decomposition pathway (R8), this adjustment did not have a significant effect
17
18 on the other observed species concentration time profiles.
19
20
21

22 23 **IIIc. $\text{CH}_3\text{C}(\text{O})\text{CH}_2\text{O}_2 + \text{HO}_2$: Rate Constant and Branching Fraction**

24
25 Figure 8 shows a representative dataset for concentration profiles of HO_2 ,
26
27 $\text{CH}_3\text{C}(\text{O})\text{CH}_2\text{O}_2$, and OH arising from the cross-reaction between $\text{CH}_3\text{C}(\text{O})\text{CH}_2\text{O}_2$ and HO_2
28
29 (R1). The simulated kinetics using the IUPAC recommended values⁶⁶ is also shown in
30
31 comparison to the results of the MC simulation fits obtained in this work. Unlike the
32
33 $\text{CH}_3\text{C}(\text{O})\text{CH}_2\text{O}_2$ self-reaction study, HO_2 and OH are a primary reactant and product,
34
35 respectively, and determining the branching fraction for the OH channel, R1b, is more
36
37 straightforward. Figure 8a shows the HO_2 concentration time dependence, which is in excess
38
39 over $\text{CH}_3\text{C}(\text{O})\text{CH}_2\text{O}_2$ concentrations by a factor of 4 – 6. It is the least sensitive of the three
40
41 species to changes in k_1 because the difference between the kinetic model with the IUPAC⁶⁶
42
43 recommended values and the fit values for the HO_2 kinetic profile arises primarily from the
44
45 $\text{CH}_3\text{C}(\text{O})\text{CH}_3$ rate enhancement coefficient for the HO_2 self-reaction (discussed in detail in
46
47 Section III d).
48
49
50
51

52
53 Figure 8b shows the $\text{CH}_3\text{C}(\text{O})\text{CH}_2\text{O}_2$ concentration time dependence, which was
54
55 monitored using UV absorption at 312 nm, and Figure 8c shows the OH concentration kinetics,
56
57
58
59
60

1
2
3 which was monitored using IR-WMS; both are compared to the IUPAC modeled and out fitted
4 kinetics. In the cross-reaction, as in the experimental results for the $\text{CH}_3\text{C}(\text{O})\text{CH}_2\text{O}_2$ self-
5
6 reaction, the prompt OH signal at early times is observable and in our fitted kinetics is simulated
7
8 as arising from R5b in the mechanism. In the presence of HO_2 , there is an additional prompt OH
9
10 concentration source present for the cross-reaction arising at early times from the reaction
11
12
13 between HO_2 and Cl (R11).
14



15
16
17 However, the additional OH at early times from R11 does not generate enough prompt OH to fit
18
19 the data. A branching fraction of 0.02 ± 0.01 for R5b again fits the prompt OH kinetics as shown
20
21 in Figure 8c. The fit for the branching fraction was observable in the OH kinetics as a scaling of
22
23 the OH concentrations on the timescale immediately following the prompt OH formation and
24
25 was, therefore, not influenced by the inclusion of the prompt OH formation mechanism. The rate
26
27 constant, k_1 , and branching fraction for the OH channel, k_{1b} / k_1 , were determined from the MC
28
29 fitting to be $(5.5 \pm 0.5) \times 10^{-12} \text{ cm}^3 \text{ molecule}^{-1} \text{ s}^{-1}$ and 0.30 ± 0.04 , respectively. The uncertainties
30
31 in our reported values were determined from a series of MC simulations as described in section
32
33 IIB; a representative set of histograms for the k_1 and k_{1b} / k_1 are shown in Figure 9a and 9b,
34
35 respectively. The resulting fits using these parameters are compared in Figure 8 to the model
36
37 results using the currently recommended values^{36, 66}: $k_1 = 9.0 (\pm 1.0) \times 10^{-12} \text{ cm}^3 \text{ molecule}^{-1} \text{ s}^{-1}$ and
38
39 $k_{1b} / k_1 = 0.15 \pm 0.10$. The improved agreement is clearly observable.
40
41
42
43
44
45
46
47
48
49
50
51
52
53
54
55
56
57
58
59
60

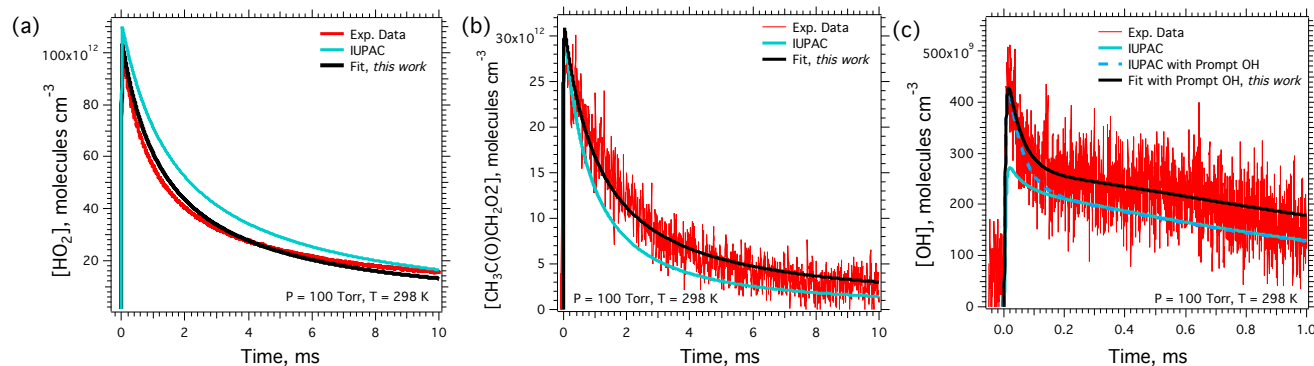


Figure 8. Experimental (a) HO_2 , (b) $\text{CH}_3\text{C}(\text{O})\text{CH}_2\text{O}_2$, and (c) OH time-dependent concentrations (red) for the $\text{HO}_2 + \text{CH}_3\text{C}(\text{O})\text{CH}_2\text{O}_2$ reaction. Uncertainties in the measured HO_2 and OH concentrations were $\pm 1.6 \times 10^{10}$ and 3.5×10^8 molecules cm^{-3} , respectively. The simulated concentrations using recommended rate parameters by IUPAC⁶⁶ (turquoise) are shown in all three panels. In panel (c) inclusion of the prompt OH (see text) is displayed (blue dashed) for comparison. The results of the fits of the temporal concentrations with the parameters from this work (black) are shown in all three panels

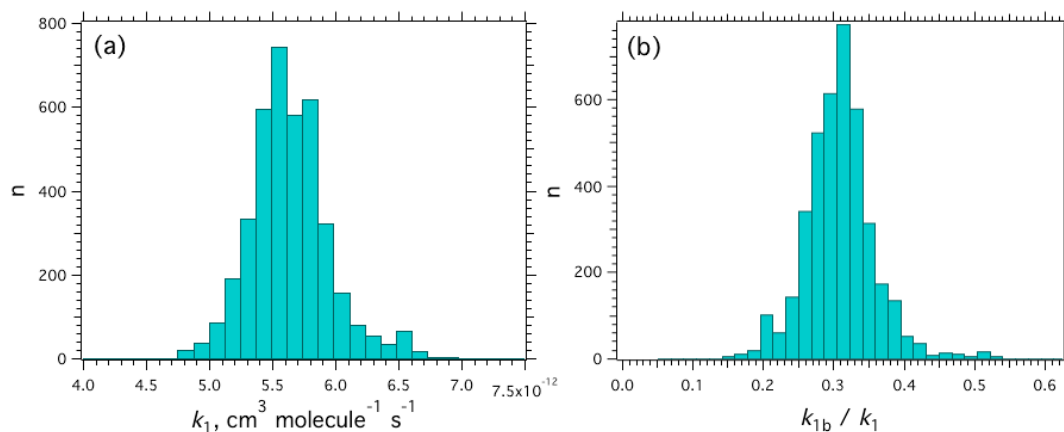


Figure 9. Histogram output from the MC simulations (4000 iterations) for (a) $k_1 = (5.5 \pm 0.5) \times 10^{-12}$ $\text{cm}^3 \text{ molecule}^{-1} \text{ s}^{-1}$ and (b) $k_{1b} / k_1 = 0.30 \pm 0.04$.

III.d. $\text{HO}_2 + \text{HO}_2$: Chaperone Effects by CH_3OH and $\text{CH}_3\text{C}(\text{O})\text{CH}_3$

A chaperone effect, increasing the rate of the self-reaction for HO_2 (R12) via H-bonded complex formation, was observed in this work.



Because a change in the effective rate constant for the HO_2 self-reaction, $k_{12,\text{obs}}$, impacts the retrieved rate constants for R1 and R2,^{31, 67, 68} it was necessary to assess its impact quantitatively in this study.

1
2
3 The chaperone rate enhancing effect by CH₃OH on R12, resulting from forming
4 HO₂•CH₃OH has been studied previously⁶⁷⁻⁶⁹ and is due to the increased reaction rate of R13
5 compared to R12.
6
7



11
12 It was shown to be negligible at room temperature and under the concentration conditions used
13 in this work because, in part, the equilibrium constant for complexation, $K_c(\text{R14})$ is small ($1.0 \times$
14 $10^{-18} \text{ cm}^3 \text{ molecule}^{-1}$) at room temperature.³⁶
15
16



20
21 To test for the effect of CH₃OH chaperone, we conducted experiments in the absence of
22 CH₃C(O)CH₃ while varying the CH₃OH concentration (see SI for details). We verify that the
23 chaperone effect from HO₂•CH₃OH was negligible. For the purpose of this work, the JPL
24 recommended value³⁶ for k_{12} ($1.55 \times 10^{-12} \text{ cm}^3 \text{ molecule}^{-1} \text{ s}^{-1}$) was used.
25
26
27
28
29
30

31 CH₃C(O)CH₃ forms a strong bond with HO₂ and its chaperone effect could be significant
32 at room temperature. Determining the effect of HO₂•CH₃C(O)CH₃ complexation on k_{12} is
33 complicated by the secondary CH₃C(O)CH₂O₂ peroxy radical chemistry. The fraction of HO₂
34 complexed as HO₂•CH₃C(O)CH₃ was included in the kinetic mechanism. The observed rate of
35 R12, $k_{12,\text{obs}}$, in the presence of CH₃C(O)CH₃ was also allowed to vary during the MC simulations
36 for determining the cross-reaction rate (k_1) and branching fraction (k_{1b}/k_1) for R1. We found
37 $k_{12,\text{obs}}$ to be statistically greater than the recommended value for k_{12} .
38
39
40
41
42
43
44
45
46

47 To test the possible chaperone enhancement by CH₃C(O)CH₃ at room temperature, a
48 series of experiments were conducted as a function of CH₃C(O)CH₃ concentration with all other
49 experimental parameters held constant. The results, shown in Figure 10, are reported as the first
50 observation of the chaperone effect rate enhancement on k_{12} at room temperature resulting from
51
52
53
54
55
56
57
58
59
60

1
2
3 HO₂•CH₃C(O)CH₃ complexation. These results build on observations reported for lower
4
5 temperatures where significant CH₃C(O)CH₃ chaperone enhancement was first observed.³⁰
6
7

8 Prior to the improvements to the IRKS system for simultaneous detection of the OH
9
10 product species described in Section IIa, analogous experiments were independently performed
11
12 and analyzed in our laboratory that investigated the chaperone effect of CH₃C(O)CH₃ on the HO₂
13
14 self-reaction. In that work, only the HO₂ and CH₃C(O)CH₂O₂ kinetic traces were observed and
15
16 analysis was done using FACSIMILE software⁷⁰ (see SI, section SVI). The lack of OH data
17
18 resulted in the k_1 rate constant and k_{1b}/k_1 branching fraction parameters being less constrained
19
20 compared to the results reported in sections IIIa and IIIb. The results of these early experiments
21
22 are reported here for the first time, also in Figure 10, together with the present data. The
23
24 CH₃C(O)CH₃ concentrations from the earlier experiments overlap with those studied here,
25
26 between $2.1\text{--}2.4 \times 10^{16}$ molecule cm⁻³, but also extend to a higher CH₃C(O)CH₃ (5.2×10^{16}
27
28 molecule cm⁻³). The two sets of data exhibit the same linear dependence of $k_{12,obs}$ with respect to
29
30 [CH₃C(O)CH₃]. The agreement between the two datasets taken years apart and analyzed through
31
32 two independent methods yields a greater confidence in the observed increased HO₂ self-reaction
33
34 rate being due to a chaperone effect. In order to consolidate the earlier datasets which did not
35
36 account for uncertainties in the overall mechanism rate constants used during the fits, a 4% total
37
38 uncertainty was used based on the MC fitting analysis (see SVI in SI for more details).
39
40
41
42
43

44 Equation 3 is the result of the combined linear fit, with each dataset weighted by their
45
46 uncertainties:
47
48

$$49 \quad k_{12,obs} = k_{12} + k''_A [(CH_3)_2CO]_0 = (1.5 \pm 0.1) \times 10^{-12} + (4.0 \pm 0.2) \times 10^{-29} \times [CH_3C(O)CH_3] \quad (E3)$$

50
51 where $k''_A = (4.0 \pm 0.2) \times 10^{-29}$ cm⁶ molecule⁻² s⁻¹ is the chaperone enhancement coefficient for
52
53 CH₃C(O)CH₃ at T = 298 K and the intercept, k_{12} , agrees with the JPL recommended value³⁶.
54
55
56
57
58
59
60

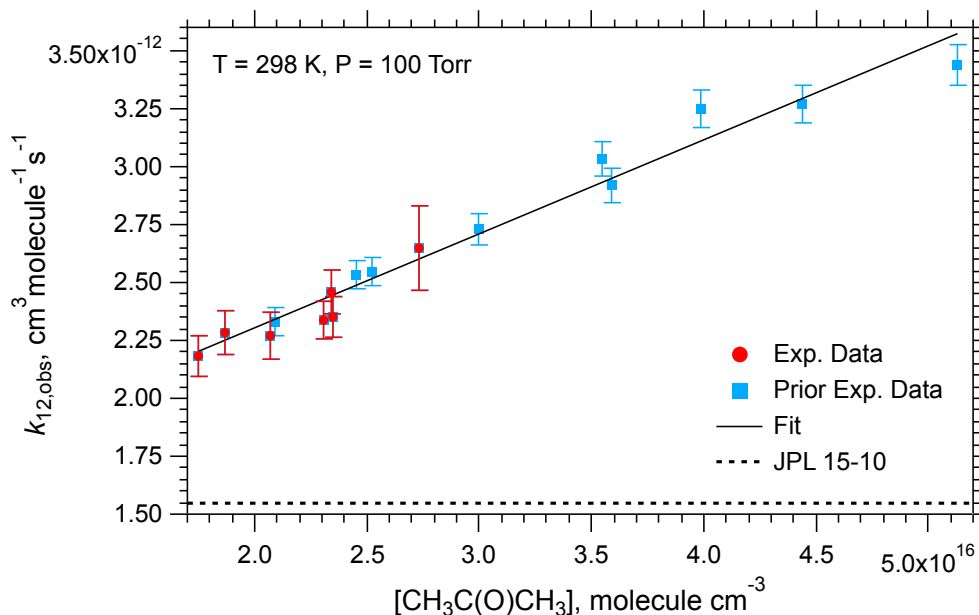
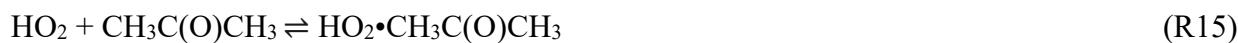


Figure 10. Experimentally determined values of $k_{12,obs}$ as a function of $\text{CH}_3\text{C}(\text{O})\text{CH}_3$ concentration. The dashed line represents the current recommended value for $k_{12,obs}$ in the JPL Data Evaluation.³⁶ Exp. Data: $k_{12,obs}$ fits obtained of current data using the Monte Carlo simulations described in Section IIb. Prior Exp. Data: $k_{12,obs}$ fits of earlier data taken before IRKS modifications fit using FACSIMILE software. The overall fit was weighted by the uncertainties in each value. ($R^2 = 0.9582$).

The magnitude of the chaperone enhancement is dependent on the relative concentration of the H-bonded $\text{HO}_2 \cdot \text{CH}_3\text{C}(\text{O})\text{CH}_3$ complex which is determined from the equilibrium constant for the formation of the complex (R15).



The complex enhances the self-reaction rate by R16.



The timescale for the attainment of equilibrium for R15 is much faster ($< 100 \mu\text{s}$) than the millisecond timescale of our kinetic observations. The recommended value³⁶ for the equilibrium constant at room temperature, $K_c(\text{R15}) = (1.4 \pm 0.84) \times 10^{-18} \text{ cm}^3 \text{ molecule}^{-1}$, is extrapolated from lower temperature studies^{31, 71} with the highest temperature for the $K_c(\text{R15})$ measurement being 272 K. $K_c(\text{R15})$ at $T = 298 \text{ K}$ can be determined directly here using the method given in Grieman

1
2
3 et al.³¹ although it is difficult to measure because of the relatively large change in initial [HO₂] at
4
5 $t = 0$ s caused by R4, the reaction of Cl with CH₃C(O)CH₃ relative to the change caused by the
6
7 complex equilibrium (R15). (See SVII in SI.) We obtain $K_c(\text{R15}) = (2.0 \pm 0.89) \times 10^{-18} \text{ cm}^3$
8
9 molecule⁻¹ ($K_{\text{eq}}(\text{R15}) = 50 \pm 22$, standard state of 1 bar) based on a weighted average of four
10
11 runs, where the uncertainty includes the propagation of all the estimated experimental errors in
12
13 addition to the standard deviation from the weighted average. The directly determined value is
14
15 40% higher than the extrapolated recommended value³⁶, but is in agreement. For the
16
17 CH₃C(O)CH₃ concentration range shown in Figure 10 for the early datasets ($2.1 - 5.1 \times 10^{16}$
18
19 molecules cm⁻³), the percent complexation of HO₂•CH₃C(O)CH₃ ranges between 4.0 – 9.2 % at
20
21 room temperature. These results as well as the rate enhancement for the HO₂ self-reaction
22
23 resulting from R15 were incorporated into the MC simulations for determining k_1 .
24
25
26
27

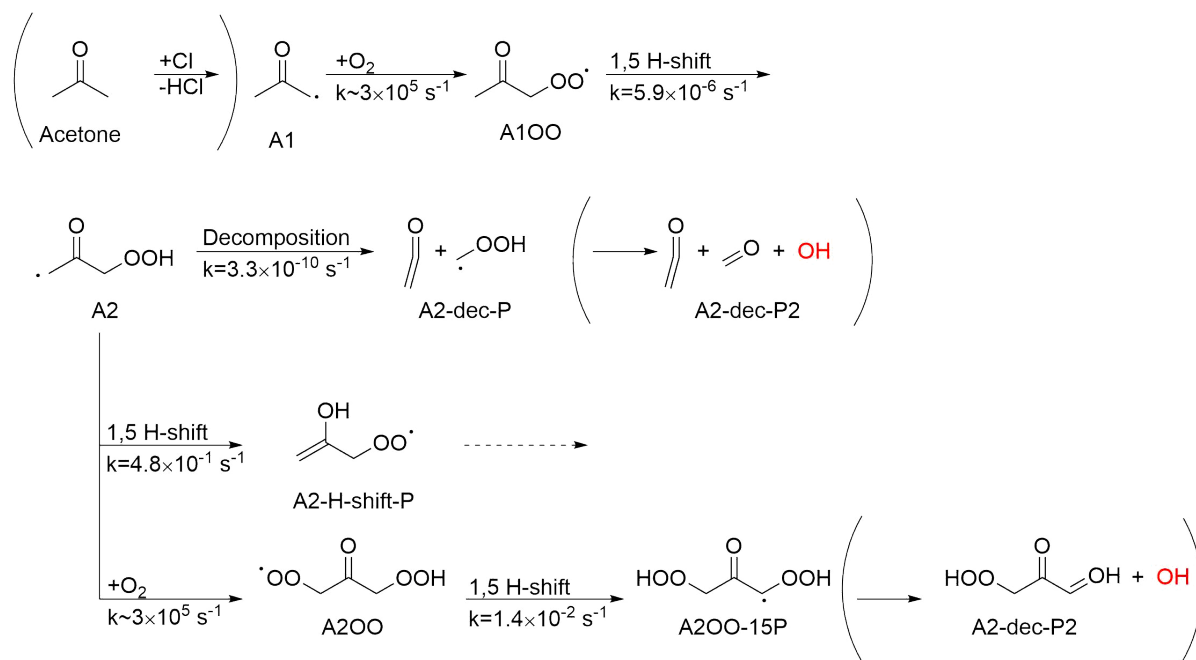
28
29 The equilibrium constant allows us to estimate the rate constant k_{16} by following the work
30
31 by Christensen et al. on the HO₂ self-reaction CH₃OH enhancement.⁶⁷ Under our conditions
32
33 where $K_c(\text{R15}) [(\text{CH}_3)_2\text{CO}] \ll 1$, and using the constants obtained from Equation 3, we obtain
34
35 k_{16} from
36

$$37 \quad k_{16} = k''_{\text{A}} / K_c(\text{R15}) + 2 k_{12} = (2.0 \pm 1.0) \times 10^{-11} \text{ cm}^3 \text{ molecule}^{-1} \text{ s}^{-1} \quad (\text{E4})$$

38
39 at room temperature, where most of the uncertainty arises from $K_c(\text{R15})$. This value is very
40
41 similar to the analogous rate constant for the HO₂•CH₃OH complex which was estimated to be
42
43 $k_{13} = (2.1 \pm 0.7) \times 10^{-11} \text{ cm}^3 \text{ molecule}^{-1} \text{ s}^{-1}$ averaged over $T = 222 - 295$ K at 100 Torr and using a
44
45 K_c averaged over $T = 230 - 260$ K.⁶⁷ Although there is no determination of the temperature
46
47 dependence of this rate constant, the magnitude of k_{16} for CH₃C(O)CH₃ at room temperature is
48
49 estimated to be the same as that for CH₃OH, k_{14} , at significantly lower temperatures where the
50
51 complex formation reactions may be faster at the same pressure.
52
53
54
55
56
57
58
59
60

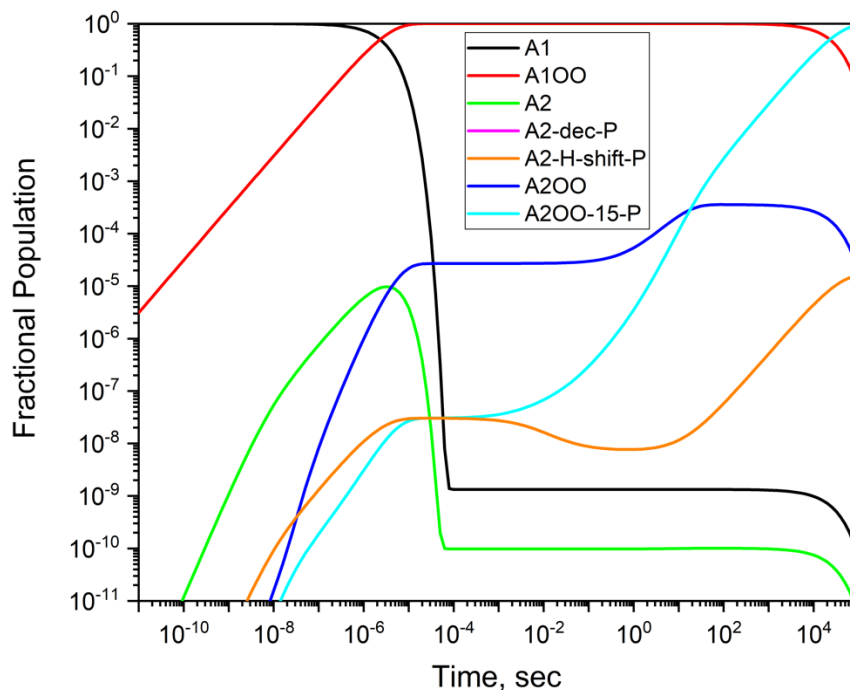
IIIe. EVALUATION OF OH GENERATION FROM THE $\text{CH}_3\text{C}(\text{O})\text{CH}_2$ RADICAL + O_2 REACTION

To assess the potential for OH formation following O_2 -addition to the $\text{CH}_3\text{C}(\text{O})\text{CH}_2$ radical, we studied the unimolecular reaction system outlined in Figure 11 starting from the $\text{CH}_3\text{C}(\text{O})\text{CH}_2$ radical (A1) with energetics as shown in Figure S4 (see SI). The reactions include those found to have the lowest barrier heights by Weidman et al.⁷² as well as an additional H-shift following a second O_2 -addition. The initial reaction is a 1,5 H-shift from the methyl group with an MC-TST calculated rate coefficient of $5.9 \times 10^{-6} \text{ s}^{-1}$. The high barrier resulting in low rate coefficient for this reaction is in agreement with previous studies^{17, 72-75} and has been ascribed to the strain in the TS induced by the sp^2 -hybridized carbon atom reducing the flexibility.⁷² This means that the 1,5 H-shift is negligible from the thermalized peroxy radical under all relevant time scales and any possible OH-recycling from reactions following this H-shift thus relies on it occurring via excess energy from the O_2 -addition to the $\text{CH}_3\text{C}(\text{O})\text{CH}_2\text{O}_2$ radical. However, in agreement with most of the previous studies,^{17, 72-74} we find that the TS for the 1,5 H-shift is higher in energy than the separated $\text{CH}_3\text{C}(\text{O})\text{CH}_2$ radical and O_2 (by 3.8 kcal mol^{-1} according to our calculations) and as shown in Figure 12, that means that the H-shift reaction does not occur via excess energy. Thus OH formation based on reactions following this 1,5 H-shift seems a highly unlikely explanation for the observed OH products and currently no explanation has been found for the experimental observations. Very recent high-level results by Weidman et al.⁷² also find that formation of OH is highly unlikely from $\text{CH}_3\text{C}(\text{O})\text{CH}_2 + \text{O}_2$ under ambient conditions. This is in agreement with our calculations which shows that this also applies to our experimental conditions and when considering the possibility of a second O_2 -addition.



25
26
27
28
29
30
31

Figure 11. Overview of the reactions modelled using RRKM-ME. Reactions in parentheses are not modelled explicitly, but are assumed to occur with unity yield. MC-TST rate coefficients at 298.15 K calculated using the approach by Møller et al.⁴⁴ are given for the unimolecular reactions and estimated pseudo-first order rate coefficients for the O₂-additions are given based on the typical experimental conditions of [O₂] = 1.6 × 10¹⁸ molecule cm³ and k_{5a} from Table 2.



53
54
55
56
57
58
59
60

Figure 12. Time-dependent species population of the modelled system under the experimental conditions. Labels refer to the scheme outlined in Figure 11.

IV. DISCUSSION

This is the first study to measure $\text{CH}_3\text{C}(\text{O})\text{CH}_2\text{O}_2$, HO_2 , and OH simultaneously to determine the rate constants and branching fractions for the reaction between $\text{CH}_3\text{C}(\text{O})\text{CH}_2\text{O}_2$ and HO_2 (R1), and the $\text{CH}_3\text{C}(\text{O})\text{CH}_2\text{O}_2$ self-reaction (R2). As shown in Table 3, prior experimental studies on this system are scarce where the study by Bridier et al (1993)²¹ was the sole paper to measure both rate constants for these reactions. In contrast to their work, the results presented here are not subject to the disadvantage of relying solely on UV absorption techniques, specifically the deconvolution of the UV traces with high uncertainty in the absorption cross-sections. In addition, the chaperone mechanism that we have shown to be substantial was not previously considered. Subsequent work measuring the branching fractions for R1 and R2 through detection of OH relied on the rate constants measured by Bridier et al. (1993) and, therefore, are subject to the same systematic errors. Indeed, the branching fractions reported in the literature for this cross-reaction and self-reaction ranged from 0.15 – 0.67 and 0.50 – 0.75, respectively, indicating that measurements for this system were poorly constrained. By independently re-measuring $\sigma_{\text{CH}_3\text{C}(\text{O})\text{CH}_2\text{O}_2}$ in a region where other species absorptions are minimal, characterizing the chaperone effects, and measuring the three species simultaneously, this work is less susceptible to the systematic errors of the previous studies.

Table 3: Summary of Experimental and Theoretical Kinetic Rate Constants and Branching Fractions for R1 and R2.

Ref. , year P (Torr), T (K)	Method	k_1	Branching Fractions, k_1^{-1}		k_2	Branching Fractions, k_2^{-1}		
			R1a	R1b		R2a	R2b	R2c
[25], 1990 760, 298	PR, UVA	-	-	-	8.3 (1.6)	-	-	-
[20], 1993 760, 298	FP, UVA	9.0 (1.0)	-	-	8.0 (2.0)	-	0.75 (0.10)	-
[19], 2004 800, 298	FTIR, HPLC, F	-	0.33 (0.13)	0.67 (0.20)	-	-	-	-
[14], 2008 700, 296	UVP, FTIR	-	-	0.15 (0.08)	-	-	-	-

1
2
3
4
5
6
7
8
9
10
11
12
13
14
15
16
17
18
19
20
21
22
23
24
25
26
27
28
29
30
31
32
33
34
35
36
37
38
39
40
41
42
43
44
45
46
47
48
49
50
51
52
53
54
55
56
57
58
59
60

[17], 2008 75–530, 298	PLP, LIF	-	-	~0.15	-	-	-	-
[26], 2003 765, 298	UVP, GC	-	-	-	-	-	0.50 (0.05)	-
[15], 2005 1–760, 298	CBS-QB3// B3LYP/6- 311G(2d,d,p) RRKM-ME		0.79	0.21				
[18], 2012 800, 295	UVP, FTIR, HPLC	-	0.75 (0.13)	0.25 (0.13)	-	-	-	-
[27], 2019 750, 297	MS	-	-	-	-	-	-	0.16‡
this work 100, 298	PLP, UVA, IR-WMS	5.5 (0.5)	0.70 (0.04)	0.30 (0.04)	4.8 (0.8)	0.37*	0.33 (0.13)	0.30†
JPL 15-10		9.0 (1.0)	-	-	-	-	-	-
IUPAC		9.0 (1.0)	0.85 (0.1)	0.15 (0.1)	8.0 (0.3)	-	0.63 (0.20)	-

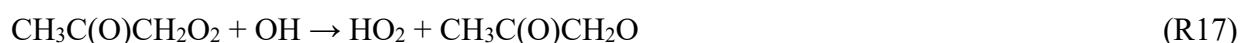
Notes: Rate constants units = 10^{-12} cm³ molecule⁻¹ s⁻¹. Reported uncertainties are in parentheses. PR = pulsed radiolysis; FP= flash photolysis; UVA = UV absorption spectroscopy; FTIR = Fourier transform infrared spectroscopy; HPLC = high-performance liquid chromatography; F = fluorescence detection; PLP = pulsed laser photolysis, LIF = laser induced fluorescence; UVP = UV Photolysis; GC = gas chromatography, MS = mass-spectrometric techniques, IR-WMS = infrared wavelength modulated spectroscopy, RRKM-ME = Rice-Ramsperger-Kassel-Marcus Master Equation.

‡Ratio based on the IUPAC recommended rate constant,⁶⁶ uncertainties not reported.

†Ratio based on overall rate constant, k_2 , from this work.

The rate constants for both the $\text{CH}_3\text{C}(\text{O})\text{CH}_2\text{O}_2$ reaction with HO_2 (k_1) and the $\text{CH}_3\text{C}(\text{O})\text{CH}_2\text{O}_2$ self-reaction (k_2) are both smaller than previously reported by Bridier et al. by about 60%. A possible explanation for this systematic difference is that the UV cross-sections used in the work by Bridier et al. were up to 40 – 60% higher than those determined in this work and those found by other studies.^{26, 29} A larger cross-section would result in a larger rate constant. Their method also required that the concentration time dependence of multiple species be de-convoluted from UV spectra, which is susceptible to the uncertainties arising in the absorption cross-sections from all of these species, particularly those arising from secondary chemistry (such as $\text{CH}_3(\text{O})\text{O}_2$, CH_3O_2 , and O_3 , as shown in the SI). To overcome these challenges, our approach was to accurately re-measure absorption cross-section values for $\text{CH}_3\text{C}(\text{O})\text{CH}_2\text{O}_2$, monitor $[\text{CH}_3\text{C}(\text{O})\text{CH}_2\text{O}_2]$ at a wavelength where no other species absorbs, and to simultaneously monitor key species independently using IR-WMS (for which uncertainties are lower) to better constrain the analysis.

1
2
3 An additional reaction mechanism that has not been considered in previous studies
4
5 involving $\text{CH}_3\text{C}(\text{O})\text{CH}_2\text{O}_2$ is the reaction between $\text{CH}_3\text{C}(\text{O})\text{CH}_2\text{O}_2$ and OH radicals. The reaction
6
7 between RO_2 and OH reaction has been observed for CH_3O_2 , $\text{C}_2\text{H}_5\text{O}_2$, $\text{C}_3\text{H}_7\text{O}_2$, and $\text{C}_4\text{H}_9\text{O}_2$, but
8
9 there is currently no experimental or theoretical evidence of this reaction for $\text{CH}_3\text{C}(\text{O})\text{CH}_2\text{O}_2$.¹⁰
11
12 The potential implications of the OH radical reaction, R17, on the rate parameter values reported
13
14 in this work have been assessed by adding R17 to the overall reaction mechanism (Table 1).
15



16
17 An estimated rate of $(5 \pm 4) \times 10^{-11} \text{ cm}^3 \text{ molecule}^{-1} \text{ s}^{-1}$ and HO_2 product formation was used based
18
19 on recent work for this class of reactions. The mean value for the rate and branching fraction for
20
21 R1 were unaffected by the addition of R17 in the MC simulations. However, the uncertainty in k_1
22
23 and k_{1b} / k_1 scaled with the input uncertainty for R17. As this was highly subjective, it was not
24
25 included in the final analysis of this work. Indeed, more work is necessary to understand the
26
27 reaction rates and product formation channels for this class of reactions and it is beyond the
28
29 scope of this work.
30
31
32
33
34

35 The branching fractions for the OH formation from R1 determined in this work fall
36
37 within the large range of values observed previously.^{15, 18-20} However, we observe a factor of two
38
39 more OH formation for this reaction than the IUPAC recommendation.⁶⁵ This is not surprising,
40
41 because the larger rate constant, k_1 , used in previous analyses is directly coupled to the absolute
42
43 magnitude of the [OH] time dependence. The larger rate constant affects the model by generating
44
45 OH at relatively faster times where secondary species concentrations that affect the OH loss are
46
47 smaller. Effectively, a higher observed [OH] would correspond to a smaller branching fraction in
48
49 the model when using the larger rate constant. Although the branching fraction determined in
50
51 this work is twice the currently recommended value, it is more consistent with the OH yields
52
53
54
55
56
57
58
59
60

1
2
3 from other peroxy radical + HO₂ experiments involving radicals with similar carbon number
4
5 (*e.g.* CH₃C(O)O₂, C₂H₅(O)O₂, C₃H₇(O)O₂, and CH₃C(O)CH₂O₂).^{36, 66, 76} In comparison to the
6
7 work by Hasson et al. (2004)²⁰, where the branching fraction was observed to be much higher
8
9 (but also with higher error) than we observe, higher concentrations of CH₃C(O)CH₂O₂ relative to
10
11 HO₂ were used by an average factor of 2. This would make their results more susceptible to
12
13 uncertainties in the CH₃C(O)CH₂O₂ self-reaction rate parameters which was not reinvestigated in
14
15 their work.
16
17

18
19 The branching fraction for the alkoxy formation from the CH₃C(O)CH₂O₂ self-reaction,
20
21 R2, is lower than that observed by Bridier et al, Emricha and Warneck, and the corresponding
22
23 IUPAC recommended value which is an average of the two works.^{21, 27, 66} The work by Bridier et
24
25 al. deconvoluted overlapping UV kinetic traces as previously discussed and the work by Emricha
26
27 and Warneck monitored yields of PAN formed after adding NO₂ to the system. In the latter, PAN
28
29 was the only detected species and the yields were expected to be from the reaction of NO₂ with
30
31 CH₃C(O)O₂ which are formed in the decomposition of CH₃C(O)CH₂O (R2b). However, NO₂ can
32
33 also react with CH₃C(O)CH₂O₂ to form an organic nitrate, which complicated their analysis. As a
34
35 result of this complexity, they used their results to provide an upper limit on the branching
36
37 fraction, which was ultimately lower than the values reported by Bridier et al. The reason for the
38
39 discrepancy between our results and the literature values is uncertain; however, our direct
40
41 detection of HO₂ and OH is a more constrained tracking of the CH₃C(O)CH₂O pathway and
42
43 reduces uncertainties in UV cross-sections and complex side chemistry resulting from nitrate
44
45 formation.
46
47
48
49

50
51 All experimental data in this work showed evidence for prompt OH formation. This was
52
53 modeled in the kinetic fits using the CH₃C(O)CH₂ + O₂ reaction (R5b). However, there is
54
55
56
57
58
59
60

1
2
3 currently no evidence for a mechanism for OH generation from this reaction based on the
4
5 theoretical work reported here as well as in recent studies.^{17, 72-74} The Cl + HO₂ reaction cannot
6
7 resolve the discrepancy because prompt OH is observed when investigating the CH₃C(O)CH₂O₂
8
9 self-reaction. The possibility of contamination in the CH₃C(O)CH₃ sample was considered. A
10
11 maximum contamination in the CH₃C(O)CH₃ sample (0.1%) with an absorption cross-section of
12
13 10⁻¹⁸ (λ = 351 nm) under our experimental conditions leading to 100% OH product would only
14
15 yield [OH] ~ 1 × 10¹¹ molecule cm⁻³ when photolyzed. In the instance that the maximum potential
16
17 OH concentration arising from an impurity would be achieved and, it is still not enough to
18
19 explain our experimental observations which averaged higher prompt OH concentrations.
20
21
22 Therefore, the observed prompt OH generation remains unexplained.
23
24
25

26 Finally, the chaperone effect of CH₃C(O)CH₃ on the HO₂ self-reaction observed in this
27
28 work can be compared to a previous study at lower temperatures³¹ as well as to the CH₃OH
29
30 chaperone effect which has been studied more extensively.⁶⁷⁻⁶⁹ The first observation of the
31
32 CH₃C(O)CH₃ chaperone mechanism enhancement was described by Grieman et al.³¹ at
33
34 significantly lower temperatures and reported a preliminary enhancement coefficient greater than
35
36 that for CH₃OH. The work presented here shows the same trend at room temperature under our
37
38 concentration conditions where the enhancement coefficient due to CH₃C(O)CH₃ complexation
39
40 with HO₂ is seen to be approximately three times greater compared to the analogous case with
41
42 CH₃OH. In fact, even at room temperature it is easily observable for CH₃C(O)CH₃, whereas it is
43
44 considered negligible for CH₃OH.
45
46
47

48
49 For further comparison, the analogous enhancement coefficient for H₂O at room temperature is
50
51 $k''_{\text{H}_2\text{O}} = (0.6 \pm 0.42) \times 10^{-29} \text{ cm}^6 \text{ molecule}^{-2} \text{ s}^{-1}$,⁶⁸ approximately an order of magnitude smaller
52
53 than that observed for CH₃C(O)CH₃. The chaperone effect parameters for CH₃C(O)CH₃ are
54
55
56
57
58
59
60

presented in Table 4 along with those for CH₃OH for comparison. Part of the reason for the greater enhancement of the HO₂ self-reaction, for CH₃C(O)CH₃ compared to CH₃OH, is the larger equilibrium constant for the formation of the hydrogen-bonded complex (K_c(R15)/K_c(R14) = 2). However, the rate constants for the reactions of HO₂ with the respective hydrogen-bonded complexes appear to be approximately the same, but the temperature dependence for these values is unknown. More experimental work is needed and an opportunity for a theoretical explanation is apparent. Regardless, the increased reaction rate for the HO₂ self-reaction must be considered in laboratory studies of kinetics involving HO₂ in the presence of significant concentrations of CH₃C(O)CH₃, even at room temperature. At lower temperatures, particularly those relevant to the tropopause, the chaperone effect has been observed to greatly increase³¹ and needs to be considered in environments containing CH₃C(O)CH₃. We are currently undertaking a thorough study of the temperature dependence of this effect on HO₂ and CH₃C(O)CH₂O₂ chemistry. It should also be noted that no acetone concentration dependence and, therefore, no chaperone dependence was found for the cross-reaction between HO₂ and CH₃C(O)CH₂O₂ (R1). (See S12 in the SI.)

Table 4. Parameters related to the chaperone effect that enhances the HO₂ self-reaction rate via the reaction with the H-bonded complexes formed between HO₂ and CH₃C(O)CH₃ (this work) or CH₃OH. Our values found for CH₃C(O)CH₃ at 298 K are compared to those previously found for CH₃OH.

Parameter	HO ₂ •CH ₃ C(O)CH ₃	Parameter	HO ₂ •CH ₃ OH
k''_A (cm ⁶ molecule ⁻² s ⁻¹)	$(4.0 \pm 0.2) \times 10^{-29}$	k''_M (cm ⁶ molecule ⁻² s ⁻¹)	$(1.09^{+2.7}_{-.99}) \times 10^{-29}$ ^a $(1.52 \pm 0.69) \times 10^{-29}$ ^b
K _c (R15) (cm ³ molecule ⁻¹) (measured)	$(2.0 \pm 0.89) \times 10^{-18}$	K _c (R14) (cm ³ molecule ⁻¹) (recommended)	1.0×10^{-18} ^c
(recommended)	$(1.4 \pm 0.84) \times 10^{-18}$ ^c		

k_{16} ($\text{cm}^3 \text{ molecule}^{-1} \text{ s}^{-1}$)	$(2.0 \pm 1.0) \times 10^{-11}$	k_{13} ($\text{cm}^3 \text{ molecule}^{-1} \text{ s}^{-1}$)	$(2.1 \pm 0.7) \times 10^{-11}$ ^{a,d}
Range of % (H-bonded complex)	(4.0 – 9.2)	Range of % (H-bonded complex)	(0.36 – 0.70)
$[(\text{CH}_3)_2\text{CO}]$ (molecule cm^{-3})	$(2.1 - 5.1) \times 10^{16}$	$[\text{CH}_3\text{OH}]$ (molecule cm^{-3})	$(3.8 - 7.5) \times 10^{15}$

^aRef. 67 ^bRef. 68; ^cRef. 35, no uncertainty reported; ^dAveraged over temperatures < 298 K (See text.)

V. CONCLUSIONS

This work measured the rate constants and branching fractions for the reactions between $\text{CH}_3\text{C}(\text{O})\text{CH}_2\text{O}_2$ and HO_2 , and the associated self-reactions by simultaneously and independently monitoring the time-dependent $\text{CH}_3\text{C}(\text{O})\text{CH}_2\text{O}_2$, HO_2 , and OH concentrations by UV absorption spectroscopy and infrared $2f$ -heterodyne detection. Kinetic simulations were used to fit the data and determine the uncertainties using a Monte Carlo algorithm. The capacity of this work to monitor three species independently and simultaneously greatly constrains the analysis and gives confidence in the results. Avoiding the need to deconvolve overlapping UV spectra by the use of IR kinetic spectroscopy of individual species results in a more straightforward analysis. The UV cross-sections for $\text{CH}_3\text{C}(\text{O})\text{CH}_2\text{O}_2$ were measured for the spectral region $\lambda = 290\text{-}320$ nm and determined to be higher than the currently recommended values³⁶ but lower than those observed by Bridier et al.²¹ The $\text{CH}_3\text{C}(\text{O})\text{CH}_2\text{O}_2$ self-reaction rate constant is $(4.8 \pm 0.8) \times 10^{-12} \text{ molecule}^{-1} \text{ cm}^3 \text{ s}^{-1}$ and the branching fraction for alkoxy formation inferred from secondary chemistry is 0.33 ± 0.13 . The rate constant is lower than the currently recommended values as is the branching fraction. It is not surprising that there is disagreement in the branching fractions considering that the previous studies for the branching fraction were not in agreement with each other and the kinetic rate was not measured in either of the two studies, but was used in their analyses. The cross-reaction between $\text{CH}_3\text{C}(\text{O})\text{CH}_2\text{O}_2$ and HO_2 experiments resulted in a rate constant and branching fraction for OH formation of $(5.50 \pm 0.53) \times 10^{-12} \text{ cm}^3 \text{ molecule}^{-1} \text{ s}^{-1}$ and

0.30 ± 0.04, respectively. This rate constant is again smaller than the previously reported value whereas the branching fraction is larger. The higher yields of OH observed in this work are more consistent with analogous reactions^{33, 36, 66, 76} and ultimately lead to less hydro peroxide product being formed from the reaction between CH₃C(O)CH₂O₂ and HO₂ than previously reported. To fit the experimentally observed OH profiles, a prompt OH formation pathway was necessary, but the mechanism for this remains unclear. The CH₃C(O)CH₃ chaperone effect had a large effect on the rate of the HO₂ self-reaction and was also required to properly fit the experimental results even at room temperature. The chaperone coefficient, $k''_A(T = 298 \text{ K}) = (4.0 \pm 0.2) \times 10^{-29} \text{ cm}^6 \text{ molecule}^{-2} \text{ s}^{-1}$, and equilibrium constant, $K_c(R15) = (2.0 \pm 0.89) \times 10^{-18} \text{ cm}^3 \text{ molecule}^{-1}$, were determined and should be considered in future peroxy experiments involving HO₂ and CH₃C(O)CH₃.

ASSOCIATED CONTENT

Supporting Information

The supporting information contains information on the instrumental calibrations, the RRKM-ME modelling, the UV absorption measurements of secondary species, the Facsimile fitting method, determination of the $K_c(15)$ equilibrium constant, and additional chaperone effects.

ACKNOWLEDGMENTS

This research was carried out by the Jet Propulsion Laboratory, California Institute of Technology, under contract with the National Aeronautics and Space Administration (NASA), supported by the Upper Atmosphere Research and Tropospheric Chemistry Programs. The contribution of K.Z. was supported by the appointment to the NASA Postdoctoral Program at the NASA Jet Propulsion Laboratory, administered by the Universities Space Research Association under contract with NASA. The contribution from A.H. was supported in part by the National Science Foundation (NSF Grant No. CHE-1413712), and the NASA Earth and Science Fellowship (NESSF). M.D.S. was supported by the NASA Earth and Space Science Fellowship (NNX16AO36H). This research was also supported by an appointment of F.J.G. to the NASA Postdoctoral Program at the Jet Propulsion Laboratory, administered by Oak Ridge Associated Universities through a contract with NASA and a SURP grant from Pomona College for E.D. The work by HGK was funded by the Independent Research Fund Denmark. **Author contributions:** S.S. and M.O. conceived and designed the research. K.Z. conducted the experiments and performed the data analysis. F.A.F. assisted with the IRKS instrumental upgrades. C.J.P. helped with experimental planning and the model mechanism. A.O.H., F.J.G., and E.D. conducted the early experiments and F.J.G. performed the data analysis on the part of

that work presented here. M.D.S. wrote the original kinetic analysis library. K.H.M. and H.G.K. contributed the RRKM-ME and MESMER modeling work. K.Z. and F.G. wrote the paper. All authors contributed to the scientific discussion and preparation of the manuscript.

REFERENCES

1. Orlando, J. J.; Tyndall, G. S. Laboratory Studies of Organic Peroxy Radical Chemistry: An Overview with Emphasis on Recent Issues of Atmospheric Significance. *Chem. Soc. Rev.* **2012**, *41*, 6294–6317.
2. Tyndall, G. S.; Cox, R. A.; Granier, C.; Lesclaux, R.; Moortgat, G. K.; Pilling, M. J.; Ravishankara, A. R.; Wallington, T. J. Atmospheric Chemistry of Small Organic Peroxy Radicals. *J. Geophys. Res.-Atmos.* **2001**, *106*, 12157–12182.
3. Vereecken, L.; Francisco, J. S. Theoretical Studies of Atmospheric Reaction Mechanisms in the Troposphere. *Chem. Soc. Rev.* **2012**, *41*, 6259–6293.
4. Kjaergaard, H. G.; Møller, K. H.; Otkjaer, R.; Wennberg, P. O.; Crouse, J.; Xu, L.; Praske, E.; Bates, K. Atmospheric Autoxidation via Fast Peroxy Radical Hydrogen Shift Reactions. *Abstracts of Papers of the Am. Chem. Soc.* **2019**, 258.
5. Crouse, J. D.; Nielsen, L. B.; Jorgensen, S.; Kjaergaard, H. G.; Wennberg, P. O. Autoxidation of Organic Compounds in the Atmosphere. *J. Phys. Chem. Lett.* **2013**, *4*, 3513–3520.
6. Wennberg, P.O.; Xu, L.; Crouse, J.; Møller, K.; Kjaergaard, H.G. Unimolecular Chemistry of Organic Peroxy Radicals in the Atmosphere. *Abstracts of Papers of the Am. Chem. Soc.* **2019**, 258.
7. Møller, K. H.; Bates, K. H.; Kjaergaard, H. G. The Importance of Peroxy Radical Hydrogen-Shift Reactions in Atmospheric Isoprene Oxidation. *J. Phys. Chem. A* **2019**, *123*, 920–932.
8. Jenkin, M. E.; Valorso, R.; Aumont, B.; Rickard, A. R. Estimation of Rate Coefficients and Branching Ratios for Reactions of Organic Peroxy Radicals for Use in Automated Mechanism Construction. *Atmos. Chem. Phys.* **2019**, *19*, 7691–7717.
9. Shallcross, D. E.; Raventos-Duran, M. T.; Bardwell, M. W.; Bacak, A.; Solman, Z.; Percival, C. J. A Semi-Empirical Correlation for the Rate Coefficients for Cross- and Self-Reactions of Peroxy Radicals in the Gas-Phase. *Atmos. Environ.* **2005**, *39*, 763–771.
10. Fittschen, C. The Reaction of Peroxy Radicals with OH radicals. *Chem. Phys. Lett.* **2019**, 725, 102–108.
11. Franco, B.; Clarisse, L.; Stavrakou, T.; Muller, J. F.; Pozzer, A.; Hadji-Lazaro, J.; Hurtmans, D.; Clerbaux, C.; Coheur, P. F. Acetone Atmospheric Distribution Retrieved From Space. *Geophys. Res. Lett.* **2019**, *46*, 2884–2893.
12. Elias, T.; Szopa, S.; Zahn, A.; Schuck, T.; Brenninkmeijer, C.; Sprung, D.; Slemr, F. Acetone Variability in the Upper Troposphere: Analysis of CARIBIC Observations and LMDz-INCA Chemistry-Climate Model Simulations. *Atmos. Chem. Phys.* **2011**, *11*, 8053–8074.
13. Fischer, E. V.; Jacob, D. J.; Millet, D. B.; Yantosca, R. M.; Mao, J. The Role of the Ocean in the Global Atmospheric Budget of Acetone. *Geophys. Res. Lett.* **2012**, *39*, L01807.
14. Khan, M. A. H.; Cooke, M. C.; Utembe, S. R.; Archibald, A. T.; Maxwell, P.; Morris, W. C.; Xiao, P.; Derwent, R. G.; Jenkin, M. E.; Percival, et al. A Study of Global Atmospheric Budget and Distribution of Acetone Using Global Atmospheric Model STOCHEM-CRI. *Atmos. Environ.* **2015**, *112*, 269–277.

- 1
2
3 15. Jenkin, M. E.; Hurley, M. D.; Wallington, T. J. Investigation of the Radical Product
4 Channel of the $\text{CH}_3\text{C}(\text{O})\text{CH}_2\text{O}_2 + \text{HO}_2$ Reaction in the Gas Phase. *Phys. Chem. Chem. Phys.*
5 **2008**, *10*, 4274–4280.
- 6 16. Hasson, A. S.; Kuwata, K. T.; Arroyo, M. C.; Petersen, E. B. Theoretical Studies of the
7 Reaction of Hydroperoxy Radicals ($\text{HO}_2\bullet$) with Ethyl peroxy ($\text{CH}_3\text{CH}_2\text{O}_2\bullet$), Acetyl peroxy
8 ($\text{CH}_3\text{C}(\text{O})\text{O}_2\bullet$) and Acetonyl Peroxy ($\text{CH}_3\text{C}(\text{O})\text{CH}_2\text{O}_2\bullet$) Radicals. *J. Photochem. Photobiol. A*
9 **2005**, *176*, 218–230.
- 10 17. Kovacs, G.; Zador, J.; Farkas, E.; Nadasdi, R.; Szilagy, I.; Dobe, S.; Berces, T.; Marta,
11 F.; Lendvay, G. Y. Kinetics and Mechanism of the Reactions of CH_3CO and $\text{CH}_3\text{C}(\text{O})\text{CH}_2$
12 Radicals with O_2 . Low-Pressure Discharge Flow Experiments and Quantum Chemical
13 Computations. *Phys. Chem. Chem. Phys.* **2007**, *9*, 4142–4154.
- 14 18. Dillon, T. J.; Crowley, J. N. Direct Detection of OH Formation in the Reactions of HO_2
15 with $\text{CH}_3\text{C}(\text{O})\text{O}_2$ and Other Substituted Peroxy Radicals. *Atmos. Chem. Phys.* **2008**, *8*, 4877–
16 4889.
- 17 19. Hasson, A. S.; Tyndall, G. S.; Orlando, J. J.; Singh, S.; Hernandez, S. Q.; Campbell, S.;
18 Ibarra, Y. Branching Ratios for the Reaction of Selected Carbonyl-Containing Peroxy Radicals
19 with Hydroperoxy Radicals. *J. Phys. Chem. A* **2012**, *116*, 6264–6281.
- 20 20. Hasson, A. S.; Tyndall, G. S.; Orlando, J. J. A Product Yield Study of the Reaction of
21 HO_2 Radicals with Ethyl Peroxy ($\text{C}_2\text{H}_5\text{O}_2$), Acetyl Peroxy ($\text{CH}_3\text{C}(\text{O})\text{O}_2$), and Acetonyl Peroxy
22 ($\text{CH}_3\text{C}(\text{O})\text{CH}_2\text{O}_2$) Radicals. *J. Phys. Chem. A* **2004**, *108*, 5979–5989.
- 23 21. Bridier, I.; Veyret, B.; Lesclaux, R.; Jenkin, M. E. Flash-Photolysis Study of the UV
24 Spectrum and Kinetics of Reactions of the Acetylperoxy Radical. *J. Chem. Soc. Faraday*
25 *Trans.* **1993**, *89*, 2993–2997.
- 26 22. Carslaw, N.; Creasey, D. J.; Harrison, D.; Heard, D. E.; Hunter, M. C.; Jacobs, P. J.;
27 Jenkin, M. E.; Lee, J. D.; Lewis, A. C.; Pilling, M. J.; et al. OH and HO_2 Radical Chemistry in a
28 Forested Region of North-Western Greece. *Atmos. Environ.* **2001**, *35*, 4725–4737.
- 29 23. Lelieveld, J.; Butler, T. M.; Crowley, J. N.; Dillon, T. J.; Fischer, H.; Ganzeveld, L.;
30 Harder, H.; Lawrence, M. G.; Martinez, M.; Taraborrelli, D.; Williams, J. Atmospheric
31 Oxidation Capacity Sustained by a Tropical Forest. *Nature* **2008**, *452*, 737–740.
- 32 24. Kubistin, D.; Harder, H.; Martinez, M.; Rudolf, M.; Sander, R.; Bozem, H.; Eerdeken,
33 G.; Fischer, H.; Gurk, C.; Klupfel, T.; et al. Hydroxyl Radicals in the Tropical Troposphere Over
34 the Suriname Rainforest: Comparison of Measurements with the Box Model MECCA. *Atmos.*
35 *Chem. Phys.* **2010**, *10*, 9705–9728.
- 36 25. Whalley, L. K.; Edwards, P. M.; Furneaux, K. L.; Goddard, A.; Ingham, T.; Evans, M. J.;
37 Stone, D.; Hopkins, J. R.; Jones, C. E.; Karunaharan, A.; et al. Quantifying the Magnitude of a
38 Missing Hydroxyl Radical Source in a Tropical Rainforest. *Atmos. Chem. Phys.* **2011**, *11*, 7223–
39 7233.
- 40 26. Cox, R. A.; Munk, J.; Nielsen, O. J.; Pagsberg, P.; Ratajczak, E. Ultraviolet-Absorption
41 Spectra and Kinetics of Acetonyl and Acetylperoxy Radicals. *Chem. Phys. Lett.* **1990**, *173*,
42 206–210.
- 43 27. Emricha, M.; Warneck, P. Branching Ratio for the Self-Reaction of Acetonyl Peroxy
44 Radicals. *Z. Naturforsch. A* **2003**, *58*, 429–433.
- 45 28. Berndt, T.; Scholz, W.; Mentler, B.; Fischer, L.; Herrmann, H.; Kulmala, M.; Hansel, A.
46 Accretion Product Formation from Self- and Cross-Reactions of RO_2 Radicals in the
47 Atmosphere. *Angew. Chem. Int. Ed.* **2018**, *57*, 3820–3824.
- 48
49
50
51
52
53
54
55
56
57
58
59
60

- 1
2
3 29. Nielsen, O. J.; Johnson, M. S.; Wallington, T. J.; Christensen, L. K.; Platz, J. UV
4 Absorption Spectra of HO₂, CH₃O₂, C₂H₅O₂, and CH₃C(O)CH₂O₂ Radicals and Mechanism of
5 the Reactions of F and Cl Atoms with CH₃C(O)CH₃. *Int. J. Chem. Kinet.* **2002**, *34*, 283–291.
- 6 30. Emricha, M.; Warneck, P. Branching Ratio for the Self-Reaction of Acetonyl Peroxy
7 Radicals. *Z. Naturforsch. A* **2003**, *58*, 429–433.
- 8 31. Grieman, F. J.; Noell, A. C.; Davis-Van Atta, C.; Okumura, M.; Sander, S. P.,
9 Determination of Equilibrium Constants for the Reaction between Acetone and HO₂ Using
10 Infrared Kinetic Spectroscopy. *J. Phys. Chem. A* **2011**, *115*, 10527–10538.
- 11 32. Hui, A. O.; Okumura, M.; Sander, S. P. Temperature Dependence of the Reaction of
12 Chlorine Atoms with CH₃OH and CH₃CHO. *J. Phys. Chem. A* **2019**, *123*, 4964–4972.
- 13 33. Hui, A. O.; Fradet, M.; Okumura, M.; Sander, S. P. Temperature Dependence Study of
14 the Kinetics and Product Yields of the HO₂ + CH₃C(O)O₂ Reaction by Direct Detection of OH
15 and HO₂ Radicals Using 2f-IR Wavelength Modulation Spectroscopy. *J. Phys. Chem. A* **2019**]
16 *123*, 3655–3671.
- 17 34. Christensen, L. E. Laboratory Studies of Atmospherically Important Gas-Phase Peroxy
18 Radical Reactions. Ph.D. Dissertation, California Institute of Technology 2002.
- 19 35. Smarte, M. D. *Modeling and Fitting of ALS MPIMS Kinetics*, v1.2.0; Caltech Data: 2019;
20 <https://data.caltech.edu/records/1248>.
- 21 36. Burkholder, J. B.; Sander, S. P.; Abbat, J. P. D.; Barker, J. R.; Huie, R. E.; Kolb, C. E.;
22 Kurylo, M. J.; Wilmouth, D. M.; Orkin, V. L.; Wine, P. H. *Chemical Kinetics and*
23 *Photochemical Data for Use in Atmospheric Studies, Evaluation No. 18*. JPL Publication 15-10:
24 Jet Propulsion Laboratory, Pasadena, 2015.
- 25 37. Levenberg, K. A Method for the Solution of Certain Non-Linear Problems in Least
26 Squares. *Quart. Appl. Math.* **1944**, *2*, 164–168.
- 27 38. Marquardt, D. An Algorithm for Least-Squares Estimation of Nonlinear Parameters. *J.*
28 *Soc. Ind. Appl. Math.* **1963**, *11*, 431–441.
- 29 39. Orlando, J. J.; Tyndall, G. S.; Vereecken, L.; Peeters, J. The Atmospheric Chemistry of
30 the Acetonyl Radical. *J. Phys. Chem. A* **2000**, *104*, 11578–11588.
- 31 40. Papadimitriou, V. C.; Karafas, E. S.; Gierczak, T.; Burkholder, J. B. CH₃CO + O₂ + M
32 (M = He, N₂) Reaction Rate Coefficient Measurements and Implications for the OH Radical
33 Product Yield. *J. Phys. Chem. A* **2015**, *119*, 7481–7497.
- 34 41. Jenkin, M. E.; Cox, R. A.; Emrich, M.; Moortgat, G. K. Mechanisms of the Cl-Atom-
35 Initiated Oxidation of Acetone and Hydroxyacetone in Air. *J. Chem. Soc. Faraday Trans.* **1993**,
36 *89*, 2983–2991.
- 37 42. Jenkin, M. E.; Hurley, M. D.; Wallington, T. J. Investigation of the Radical Product
38 Channel of the CH₃C(O)O₂ + HO₂ Reaction in the Gas Phase. *Phys. Chem. Chem. Phys.* **2007**, *9*,
39 3149–3162.
- 40 43. Veyret, B.; Lesclaux, R.; Rayez, M. T.; Rayez, J. C.; Cox, R. A.; Moortgat, G. K.
41 Kinetics and Mechanism of the Photooxidation of Formaldehyde. 1. Flash-Photolysis Study. *J.*
42 *Phys. Chem.* **1989**, *93*, 2368–2374.
- 43 44. Møller, K. H.; Otkjaer, R. V.; Hyttinen, N.; Kurten, T.; Kjaergaard, H. G. Cost-Effective
44 Implementation of Multiconformer Transition State Theory for Peroxy Radical Hydrogen Shift
45 Reactions. *J. Phys. Chem. A* **2016**, *120*, 10072–10087.
- 46 45. Halgren, T. A. Merck Molecular Force Field. 1. Basis, Form, Scope, Parameterization,
47 and Performance of MMFF94. *J. Comput. Chem.* **1996**, *17*, 490–519.
- 48 46. Spartan '18. *Wavefunction Inc., Irvine, CA* **2018**.
- 49
50
51
52
53
54
55
56
57
58
59
60

- 1
2
3 47. Lee, C. T.; Yang, W. T.; Parr, R. G. Development of the Colle-Salvetti Correlation-
4 Energy Formula into a Functional of the Electron-Density. *Phys. Rev. B* **1988**, *37*, 785–789.
- 5 48. Hehre, W. J.; Ditchfield, R.; Pople, J. A. Self-Consistent Molecular-Orbital Methods.12.
6 Further Extensions of Gaussian-Type Basis Sets for Use in Molecular-Orbital Studies of
7 Organic-Molecules. *J. Chem. Phys.* **1972**, *56*, 2257–2261.
- 8 49. Clark, T.; Chandrasekhar, J.; Spitznagel, G. W.; Schleyer, P. V. Efficient Diffuse
9 Function-Augmented Basis Sets for Anion Calculations. Iii. The 3-21+G Basis Set for First-Row
10 Elements, Li-F. *J. Comput. Chem.* **1983**, *4*, 294–301.
- 11 50. Frisch, M. J.; Trucks, G. W.; Schlegel, H. B.; Scuseria, G. E.; Robb, M. A.; Cheeseman,
12 J. R.; Scalmani, G.; Barone, V.; Petersson, G. A.; Nakatsuji, H.; et al. Gaussian 16 Revision
13 C.01. *Gaussian Inc. Wallingford CT*. **2016**.
- 14 51. Frisch, M. J.; Pople, J. A.; Binkley, J. S. Self-Consistent Molecular-Orbital Methods. 25.
15 Supplementary Functions for Gaussian-Basis Sets. *J. Chem. Phys.* **1984**, *80*, 3265–3269.
- 16 52. Becke, A. D. Density-Functional Thermochemistry. 3. The Role of Exact Exchange. *J.*
17 *Chem. Phys.* **1993**, *98*, 5648–5652.
- 18 53. Otkjær, R. V.; Møller, K. H. Removal of Duplicate Conformers.
19 <https://github.com/TheKjaergaardGroup/Removal-of-Duplicate-Conformers>.
- 20 54. Chai, J. D.; Head-Gordon, M. Optimal Operators for Hartree-Fock Exchange from Long-
21 Range Corrected Hybrid Density Functionals. *Chem. Phys. Lett.* **2008**, *467*, 176–178.
- 22 55. Dunning, T. H., Gaussian-Basis Sets for Use in Correlated Molecular Calculations. 1.
23 The Atoms Boron Through Neon and Hydrogen. *J. Chem. Phys.* **1989**, *90*, 1007–1023.
- 24 56. Kendall, R. A.; Dunning, T. H.; Harrison, R. J. Electron-Affinities of the 1st-Row Atoms
25 Revisited- Systematic Basis-Sets and Wave-Functions. *J. Chem. Phys.* **1992**, *96*, 6796–6806.
- 26 57. Dunning, T. H.; Peterson, K. A.; Wilson, A. K. Gaussian Basis Sets for Use in Correlated
27 Molecular Calculations. X. The Atoms Aluminum Ahrough Argon Revisited. *J. Chem. Phys.*
28 **2001**, *114*, 9244–9253.
- 29 58. Werner, H. J.; Knizia, G.; Manby, F. R. Explicitly Correlated Coupled Cluster Methods
30 with Pair-Specific Geminals. *Mol. Phys.* **2011**, *109*, 407–417.
- 31 59. Werner, H. J.; Knowles, P. J.; Knizia, G.; Manby, F. R.; Schutz, M. Molpro: A General-
32 Purpose Quantum Chemistry Program Package. *Wiley Interdisciplinary Reviews-Computational*
33 *Molecular Science* **2012**, *2*, 242–253.
- 34 60. Adler, T. B.; Knizia, G.; Werner, H. J. A Simple and Efficient CCSD(T)-F12
35 Approximation. *J. Chem. Phys.* **2007**, *127*, 221106.
- 36 61. Knizia, G.; Adler, T. B.; Werner, H. J. Simplified CCSD(T)-F12 Methods: Theory and
37 Benchmarks. *J. Chem. Phys.* **2009**, *130*, 054104.
- 38 62. Peterson, K. A.; Adler, T. B.; Werner, H. J. Systematically Convergent Basis Sets for
39 Explicitly Correlated Wavefunctions: The Atoms H, He, B-Ne, and Al-Ar. *J. Chem. Phys.* **2008**,
40 *128* (8).
- 41 63. Watts, J. D.; Gauss, J.; Bartlett, R. J. Coupled-Cluster Methods with Noniterative Triple
42 Excitations for Restricted Open-Shell Hartree-Fock and Other General Single Determinant
43 Reference Functions—Energies and Analytical Gradients. *J. Chem. Phys.* **1993**, *98*, 8718–8733.
- 44 64. Glowacki, D. R.; Liang, C. H.; Morley, C.; Pilling, M. J.; Robertson, S. H. MESMER:
45 An Open Source Master Equation Solver for Multi-Energy Well Reactions. *J. Phys. Chem. A*
46 **2012**, *116*, 9545–9560.
- 47 65. Eckart, C. The Penetration of a Potential Barrier by Electrons. *Phys. Rev.* **1930**, *35*,
48 1303–1309.
- 49
50
51
52
53
54
55
56
57
58
59
60

66. Atkinson, R.; Baulch, D. L.; Cox, R. A.; Crowley, R. F.; Hampson, R. F.; Hynes, M.E.; Jenkin, M. E.; Rossi, M. J.; Troe, J.; IUPAC Subcommittees, Evaluated Kinetic and Photochemical Data for Atmospheric Chemistry: Volume II – Gas Phase Reactions of Organic Species. *Atmos. Chem. Phys.* **2006**, *6*, 3625–4055.
67. Christensen, L. E.; Okumura, M.; Hansen, J. C.; Sander, S. P., Experimental and Ab Initio Study of the HO₂•CH₃OH Complex: Thermodynamics and Kinetics of Formation. *J. Phys. Chem. A* **2006**, *110*, 6948–6959.
68. Tang, Y. X.; Tyndall, G. S.; Orlando, J. J. Spectroscopic and Kinetic Properties of HO₂ Radicals and the Enhancement of the HO₂ Self Reaction by CH₃OH and H₂O. *J. Phys. Chem. A* **2010**, *114*, 369–378.
69. Stone, D.; Rowley, D. M. Kinetics of the Gas Phase HO₂ Self-Reaction: Effects of Temperature, Pressure, Water and Methanol Vapours. *Phys. Chem. Chem. Phys.* **2005**, *7*, 2156–2163.
70. Curtis, A. R.; Sweetenham, W. P. FACSIMILE/CHEKMAT, H015 ed, v. 4.1.41. *MCPA Software: Harwell, Oxfordshire, U.K.* **1987**.
71. Dillon, T. J.; Pozzer, A.; Vereecken, L.; Crowley, J. N.; Lelieveld, J. Does Acetone React with HO₂ in the Upper-Troposphere? *Atmos. Chem. Phys.* **2012**, *12*, 1339–1351.
72. Weidman, J. D.; Turney, J. M.; Schaefer, H. F. Energetics and Mechanisms for the Acetonyl Radical + O₂ Reaction: An Important System for Atmospheric and Combustion Chemistry. *J. Chem. Phys.* **2020**, *152*, 114301.
73. Kuwata, K. T.; Hasson, A. S.; Dickinson, R. V.; Petersen, E. B.; Valin, L. C. Quantum Chemical and Master Equation Simulations of the Oxidation and Isomerization of Vinyloxy Radicals. *J. Phys. Chem. A* **2005**, *109*, 2514–2524.
74. Hassouna, M.; Delbos, E.; Devolder, P.; Viskolcz, B.; Fittschen, C. Rate and Equilibrium Constant of the Reaction of 1-Methylvinyloxy Radicals with O₂: CH₃COCH₂ + O₂ → CH₃COCH₂O₂. *J. Phys. Chem. A* **2006**, *110*, 6667–6672.
75. El-Nahas, A. M.; Simmie, J. M.; Navarro, M. V.; Bozzelli, J. W.; Black, G.; Curran, H. J. Thermochemistry and Kinetics of Acetonylperoxy Radical Isomerisation and Decomposition: A Quantum Chemistry and CVT/SCT Approach. *Phys. Chem. Chem. Phys.* **2008**, *10*, 7139–7149.
76. Winiberg, F. A. F.; Dillon, T. J.; Orr, S. C.; Gross, C. B. M.; Bejan, I.; Brumby, C. A.; Evans, M. J.; Smith, S. C.; Heard, D. E.; Seakins, P. W. Direct Measurements of OH and Other Product Yields From the HO₂ + CH₃C(O)O₂ Reaction. *Atmos. Chem. Phys.* **2016**, *16*, 4023–4042.

TOC Graphic:

